

A chip-scale polarization-spatial-momentum quantum SWAP gate in silicon nanophotonics

Received: 10 March 2022

Accepted: 27 April 2023

Published online: 15 June 2023

 Check for updates

Xiang Cheng^{1,9}, Kai-Chi Chang^{1,9}, Zhenda Xie^{1,2,3,9},
Murat Can Sarihan¹, Yoo Seung Lee¹, Yongnan Li¹, XinAn Xu²,
Abhinav Kumar Vinod¹, Serdar Kocaman^{2,4}, Mingbin Yu^{5,6},
Patrick Guo-Qiang Lo^{5,7}, Dim-Lee Kwong⁵, Jeffrey H. Shapiro⁸,
Franco N. C. Wong⁸ & Chee Wei Wong^{1,2}

Recent progress in quantum computing and networking has enabled high-performance, large-scale quantum processors by connecting different quantum modules. Optical quantum systems show advantages in both computing and communications, and integrated quantum photonics further increases the level of scaling and complexity. Here we demonstrate an efficient SWAP gate that deterministically swaps a photon's polarization qubit with its spatial-momentum qubit on a nanofabricated two-level silicon photonics chip containing three cascaded gates. The on-chip SWAP gate is comprehensively characterized by tomographic measurements with high fidelity for both single-qubit and two-qubit operation. The coherence preservation of the SWAP gate process is verified by single-photon and two-photon quantum interference. The coherent reversible conversion of our SWAP gate facilitates examinations of a quantum interconnect between two chip-scale photonic subsystems with different degrees of freedom, now demonstrated by distributing four Bell states between the two chips. We also elucidate the source of decoherence in the SWAP operation in pursuit of near-unity fidelity. Our deterministic SWAP gate in the silicon platform provides a pathway towards integrated quantum information processing for interconnected modular systems.

Over the past few decades, quantum computing has undergone tremendous advances in the realization of quantum supremacy^{1,2} on a range of physical platforms^{3,4}. Optical quantum systems are a leading platform for achieving practical optically interconnected and distributed quantum computation⁵, which has been demonstrated to be scalable, in principle, with only linear optics⁶. Photons are potentially free

from decoherence and are easily manipulated in multiple degrees of freedom⁷, and effective interactions between photons are needed to construct an optical quantum computer realizable with optical quantum gates⁸. Universal quantum computing requires both single-qubit and two-qubit gate operations, the latter of which are usually probabilistic, leading to a large resource overhead that scales exponentially

¹Fang Lu Mesoscopic Optics and Quantum Electronics Laboratory, University of California, Los Angeles, CA, USA. ²Optical Nanostructures Laboratory, Columbia University, New York, NY, USA. ³National Laboratory of Solid State Microstructures and School of Electronic Science and Engineering, Nanjing University, Nanjing, China. ⁴Department of Electrical Engineering, Middle East Technical University, Ankara, Turkey. ⁵Institute of Microelectronics, Singapore, Singapore. ⁶State Key Laboratory of Functional Materials for Informatics, Shanghai Institute of Microsystem and Information Technology, and Shanghai Industrial Technology Research Institute, Shanghai, China. ⁷Advanced Micro Foundry, Singapore, Singapore. ⁸Research Laboratory of Electronics, Massachusetts Institute of Technology, Cambridge, MA, USA. ⁹These authors contributed equally: Xiang Cheng, Kai-Chi Chang, Zhenda Xie.  e-mail: chengxiang@ucla.edu; uclakcchang@ucla.edu; cheewei.wong@ucla.edu

with the number of gates. Although cluster-state quantum computing has been proposed to drastically reduce resource overhead compared to the standard model^{9,10}, these cluster states cannot be prepared deterministically, and the probabilistic quantum-gates-associated resource overhead remains high¹¹. On the other hand, deterministic linear-optical quantum gates have been demonstrated utilizing several degrees of freedom (DoFs) of a single photon for multiple-qubit encoding¹². This scheme is equivalent to performing a unitary operation on a multidimensional qubit (or qudit) encoded into a single photon, and thus can be implemented with linear optics¹³. Such a deterministic two-qubit quantum gate will be beneficial for realizing a large-scale optical quantum computer due to its low resource overhead and high intrinsic success rate.

Optical quantum systems also provide a natural integration of quantum computation and quantum communication, which is promising regarding the ultimate goal of building a quantum internet^{14,15}. The quantum internet will enable quantum communications among remote quantum devices via quantum links, which will substantially scale up the number of qubits for distributed quantum computing¹⁶. Photonics channels can establish quantum links between distant stationary nodes with minimal loss and decoherence over long distances. Due to photons' well-defined Hilbert space in multiple DoFs, they are suitable for interconnecting with a range of photonic platforms and increasing communications rates with high-dimensional encoding^{17,18}. The recently developed integrated quantum photonics has opened another avenue for scaling up, and, taking advantage of wafer-scale fabrication processes, a state-of-the-art large-scale quantum device with more than 550 optical components has been demonstrated for multidimensional entanglement^{19,20}. These large-scale integrated photonics can increase the scale and complexity of quantum circuits, and a universal two-qubit unitary operation has been demonstrated that exploits high-dimensional entanglement in the path DoFs²¹.

Exploiting the photonics platform with a commercially available complementary metal-oxide-semiconductor (CMOS)-compatible process, we demonstrate an efficient silicon SWAP gate that deterministically swaps the polarization qubit with the spatial-momentum qubit from a single photon. The polarization DoF is easy to manipulate and measure using just waveplates and polarizing components, and the spatial-momentum DoF is naturally compatible with integrated photonics for path encoding and manipulation¹⁹. Our on-chip SWAP gate accesses these two DoFs by a concatenated scheme of three integrated controlled NOT gates: a specially designed momentum-controlled NOT (MC-NOT) gate sandwiched by two polarization-controlled NOT (PC-NOT) gates, with the two-stage MC-NOT gate nanofabricated in a self-aligned two-level silicon photonic process. We characterize the on-chip SWAP gate via state and process tomography with high fidelity for both single-qubit and two-qubit operation, with a single-qubit swapping process fidelity of up to $95.5 \pm 0.1\%$ and two-qubit swapping process fidelity of up to $94.9 \pm 2.0\%$. The preservation of quantum coherence in the on-chip SWAP operation of our silicon gate is verified by two-photon interference. The phase coherence of the on-chip SWAP operation is examined by single-photon self-interference with long-term stability. Furthermore, the reversible coherent conversion between the polarization and spatial-momentum qubits of our on-chip SWAP gate enables quantum interconnects. Enabled by the good single-chip performance, we demonstrate the quantum photonic interconnectivity by distributing four Bell states between two SWAP gates with a measured averaged Bell-state fidelity of $91.5 \pm 0.8\%$ in the polarization DoF after the second chip. Using a theoretical model, we also elucidate the source of possible errors for our silicon SWAP gate, including imperfect qubit rotation, spatial-mode contamination and unbalanced photon loss, and find good agreement with the measured truth-table fidelity of the on-chip SWAP operation. Our chip-scale deterministic SWAP gate provides unitary operation in the control of single and entangled photons, and its coherent reversible conversion

enables a quantum photonic interconnect that will facilitate future distributed and cloud quantum computing^{22–24}.

Results

SWAP gate configuration and chip implementation

Figure 1a, left panel, presents a logic circuit schematic of the SWAP gate operation that swaps arbitrary values of qubits A and B without measuring or perturbing them. When qubits A and B are respectively encoded in the polarization and spatial-momentum modes of a single photon, a SWAP gate operation can be realized with the three-gate cascade shown in Fig. 1a, right panel²⁵. In probabilistic linear-optical quantum processing, most of the quantum logic operations are performed on two qubits, usually qubits of the same modality from two different photons. Here, a SWAP gate can coherently exchange states non-deterministically between qubits residing on different photons. In our single-photon two-qubit SWAP gate, qubit states are exchanged deterministically between the polarization and spatial-momentum DoFs of the same photon, which suggests that robust on-chip multi-qubit single-photon logic of higher order should be achievable^{26–29}.

The polarization qubit (P) is based on the two polarization eigenstates $|H\rangle$ and $|V\rangle$, which correspond to the transverse electric (TE) and transverse magnetic (TM) polarizations of our quantum photonic chip. Our experiments use a type-II phase-matched spontaneous parametric downconversion (SPDC) waveguide source that produces $|V_S H_I\rangle$ biphotons in a single spatial mode, where the subscripts S and I denote the signal and idler qubits. The momentum qubit (M) is based on two spatial-momentum eigenstates $|T\rangle$ and $|B\rangle$, which correspond to the top and bottom channels of the quantum chip. Our experiments illuminate either the SWAP chip's top or bottom channels with polarization-rotated signal photons from the SPDC source, resulting in input state $|\Psi_T\rangle_{\text{IN}} = (|T_S H_S\rangle + e^{i\phi} |T_S V_S\rangle) \otimes |H_I\rangle / \sqrt{2}$ for top-channel illumination and $|\Psi_B\rangle_{\text{IN}} = (|B_S H_S\rangle + e^{i\phi} |B_S V_S\rangle) \otimes |H_I\rangle / \sqrt{2}$ for bottom-channel illumination, where $|H_I\rangle$ acts as a herald for the two qubits contained in its signal-photon companion. Defining $|0_{\text{PS}}\rangle = |H_S\rangle$, $|1_{\text{PS}}\rangle = |V_S\rangle$, $|0_{\text{MS}}\rangle = |T_S\rangle$ and $|1_{\text{MS}}\rangle = |B_S\rangle$ to be the logical-basis states, the input states become $|\Psi_T\rangle_{\text{IN}} = (|0_{\text{MS}} 0_{\text{PS}}\rangle + e^{i\phi} |0_{\text{MS}} 1_{\text{PS}}\rangle) \otimes |H_I\rangle / \sqrt{2}$ and $|\Psi_B\rangle_{\text{IN}} = (|1_{\text{MS}} 0_{\text{PS}}\rangle + e^{i\phi} |1_{\text{MS}} 1_{\text{PS}}\rangle) \otimes |H_I\rangle / \sqrt{2}$, which result in output states $|\Psi_T\rangle_{\text{OUT}} = (|1_{\text{MS}} 1_{\text{PS}}\rangle + e^{i\phi} |0_{\text{MS}} 1_{\text{PS}}\rangle) \otimes |H_I\rangle / \sqrt{2}$ and $|\Psi_B\rangle_{\text{OUT}} = (|1_{\text{MS}} 0_{\text{PS}}\rangle + e^{i\phi} |0_{\text{MS}} 0_{\text{PS}}\rangle) \otimes |H_I\rangle / \sqrt{2}$ respectively. The signal photon's polarization and spatial-momentum qubits have been swapped and undergone a bit-flip.

The preceding SWAP operation is accomplished in our silicon photonics platform with three cascaded C-NOT gates designed so that the control and target qubits exchange roles in the middle C-NOT gate³⁰, as depicted in Fig. 1a, right panel. In our architecture, the PC-NOT gates are realized by a silicon-photonics polarized directional coupler, as shown in Fig. 1b. The silicon MC-NOT gate is realized by a specially designed two-layer polarization structure that, as shown in Fig. 1c, consists of two stages: (1) a polarization rotation stage, which tapers and rotates the qubit polarization by 90° , and (2) a polarization-maintaining mode conversion stage, which converts the qubit mode profile to match the output waveguide. The polarization rotation stage is shown in Fig. 1d. Because the polarization rotation and mode conversion are only implemented for the top channel, as shown in Fig. 1f, the two-layer polarization structure thus performs the MC-NOT operation. Detailed design-space maps and optimization of the MC-NOT and PC-NOT gates are described in Supplementary Section I.

Each of the PC-NOT and MC-NOT gates has a silicon-dioxide top cladding, with a rectangular silicon waveguide with a $460 \text{ nm} \times 220 \text{ nm}$ width-height cross-section, and with relatively small birefringence between the TE and TM modes for the polarization operations and diversity^{31,32}. The optimized PC-NOT gate has a waveguide-to-waveguide gap of 400 nm with a designed $11.5\text{-}\mu\text{m}$ coupling length, ensuring that the TE mode remains in its original waveguide while the TM mode

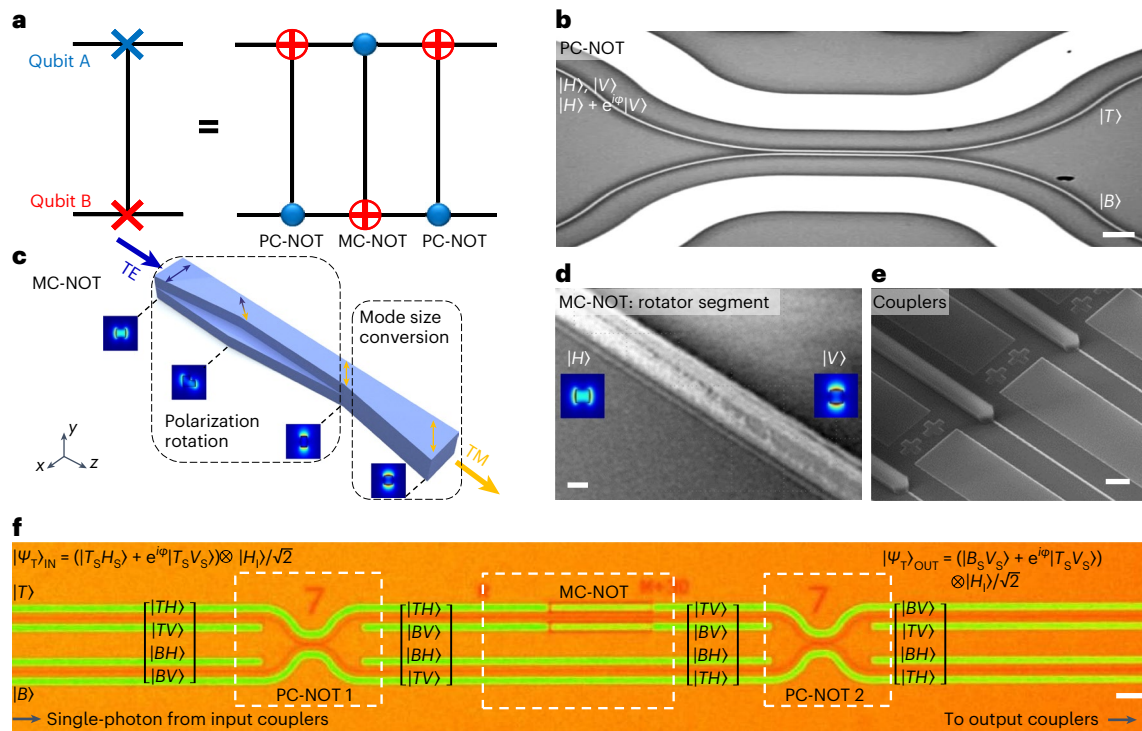


Fig. 1 | A chip-scale polarization-spatial single-photon two-qubit SWAP gate.

a, Illustrative logic circuit of the two-qubit SWAP gate. This can be realized for a single photon carrying qubit A in its polarization mode and qubit B in its spatial-momentum mode, by sequentially applying a PC-NOT gate, an MC-NOT gate and another PC-NOT gate, which are controlled by qubits A, B and A, respectively. **b**, Scanning electron microscopy (SEM) image of the chip-scale SWAP gate's first-stage PC-NOT gate realized by an optimized integrated-photonic polarized coupler. Scale bar, 2 μm . **c**, Schematic of an integrated two-level polarization rotator with polarization rotation and mode size conversion sections, enabling the second-stage MC-NOT gate for the SWAP

operation. **d**, SEM image of the MC-NOT gate's nanofabricated polarization rotation segment. Scale bar, 500 nm. **e**, SEM image of inverse taper couplers for improved free-space qubit-to-chip coupling. Scale bar, 20 μm . **f**, Optical micrograph of the complete SWAP gate operation using the cascaded PC-NOT/MC-NOT/PC-NOT architecture. Scale bar, 10 μm . An example of the input state $|\Psi_T\rangle_{\text{IN}} = (|T_S H_S\rangle + e^{i\phi}|T_S V_S\rangle) \otimes |H\rangle/\sqrt{2}$ for the top channel of the SWAP gate is shown, leading to the output state $|\Psi_T\rangle_{\text{OUT}} = (|B_S V_S\rangle + e^{i\phi}|T_S V_S\rangle) \otimes |H\rangle/\sqrt{2}$, where the signal photon's polarization qubit is swapped to the spatial-momentum qubit. State vectors at each NOT gate segment represent the resulting states of each gate operation on four possible input states ($|TH\rangle, |TV\rangle, |BH\rangle, |BV\rangle$).

crosses over to the other waveguide, with an achieved average extinction ratio of -18 dB for different input-output ports and polarization combinations (details are provided in Supplementary Section II). The optimized MC-NOT gate has two 110-nm step-height layers, and with tapered widths down to 150 nm and uniform 30-nm lateral offsets. This specially designed polarization rotator requires two-level fabrication with two-mask alignment. The misalignment of the two masks (or levels) creates scattering losses and reduces the polarization extinction ratio³³, limiting the performance of the resulting MC-NOT gate and ultimately the SWAP gate. To overcome misalignment, we have developed a self-aligned two-level nanofabrication approach to achieve the high extinction ratio required for the polarization rotator (as detailed in Supplementary Section II). Two mask layers serve as the single mask for the first 220-nm silicon reactive ion etch of the whole MC-NOT gate region, then the top layer is stripped via a resist developer, leaving the already-patterned hard mask. This hard mask is already self-aligned to the first etch and thus serves as the mask to define the 110-nm etch for the polarization rotator region in Fig. 1c. This self-alignment procedure eliminates the need for alignment between the two silicon etch steps, and only two-level alignment before the first etch is needed for a relatively flat surface for lithography patterning, resulting in a guaranteed 30-nm layer-to-layer offset without alignment error. Our designed MC-NOT gate achieved a high extinction ratio of -20 dB for both TE and TM modes. The sidewall roughness is minimized for low waveguide loss, to ensure good SWAP gate performance. In addition, to ensure good coupling efficiency, adiabatic inverse tapers are designed

for mode-index transformation at the input-output facets as shown in Fig. 1e, with less than 3-dB loss for each facet.

The silicon PC-NOT and MC-NOT gates were individually characterized using a swept tunable laser (Santec TSL-510). The transmission spectra of both gates were measured using a free-space coupling system, which selects the input and output channels for the gates. The input laser light's polarization was set by a polarizer and a half-wave plate (HWP) for $|H\rangle$ or $|V\rangle$, and the output light was measured by a polarizer. The on-chip PC-NOT and MC-NOT gates were found to have extinction ratios of more than 18 dB and 20 dB, respectively, over a 100-nm span range in the C band (transmission results are detailed in Supplementary Section II). Next, we characterized the on-chip SWAP gate performance using the same coupling system for the four basis states $|TH\rangle, |TV\rangle, |BH\rangle$ and $|BV\rangle$. Consistent performance was achieved from 1,550 nm to 1,560 nm with extinction ratios of more than 12 dB (transmission results are detailed in Supplementary Section III). The crosstalk suppression of the SWAP gate is mainly bounded by the finite extinction ratios of the PC-NOT and MC-NOT gates, as well as the polarization misalignment between the output waveguide mode and the projection polarizers. The total insertion loss of the SWAP gate chip was estimated to be -6 dB; this could be further reduced by better engineering of the coupler structure³⁴.

Truth table of the on-chip SWAP gate

With sufficiently low crosstalk measured between the basis states, we next examined the heralded single-photon two-qubit SWAP operation

in the computational basis. Our single-photon two-qubit SWAP gate measurement set-up is shown schematically in Fig. 2a. Continuous-wave SPDC in a 1.5-cm ppKTP waveguide (AdvR) designed for type-II phase matching at $\sim 1,556$ nm produces orthogonally polarized signal–idler biphotons³⁵. The pump is a Fabry–Pérot laser diode stabilized with self-injection locking, through a double-pass first-order diffraction feedback with an external grating (details are provided in Supplementary Section IV)³⁶. Tunable single-longitudinal mode lasing is achieved between 775.0 nm and 793.0 nm, enabling tunable SPDC with signal wavelengths from 1,552.5 to 1,559.6 nm, as shown in the inset of Fig. 2a. A long-pass filter blocks the residual pump photons after the SPDC, and an angle-mounted bandpass filter with an optical depth of 5 to 6 and a 95% passband transmission (Semrock N1R01-1570/3) further suppresses pump photons. Here, the biphoton state $|V_s H_i\rangle$ is generated by SPDC. The signal and idler photons are then separated by the polarization beamsplitter (PBS). The signal photons are fed to the SWAP gate while the idler photons are directed to the superconducting nanowire single-photon detector (SNSPD; Photon Spot with $\sim 85\%$ detection efficiency) for heralding. A two-in two-out free-space coupling system accesses the top and bottom channels of the SWAP chip at both its input and output facets. For each input channel, half-wave (HWP), quarter-wave (QWP) and/or multi-order wave (MWP) plates control the input polarization state for each measurement set-up shown in Fig. 2a. The polarization state of the signal photon becomes $|H\rangle$ or $|V\rangle$ or the superposition state given earlier according to the waveplate combination. The input spatial-momentum state is controlled by switching the input fibre (blue dashed line) to the top or bottom channel of the SWAP gate, resulting in $|T\rangle$ or $|B\rangle$. For the truth-table measurements, the input states to our SWAP gate are in the four-dimensional Hilbert space spanned by $|TH\rangle$, $|TV\rangle$, $|BH\rangle$ and $|BV\rangle$, corresponding to $|00\rangle$, $|01\rangle$, $|10\rangle$ and $|11\rangle$ in the logical basis. Polarizers P_2 and P_3 are rotated for polarization projection at the output ports. Coincidence counting is then performed using SNSPDs at the P_2 and P_3 outputs with internal timing delays to match that of the heralding detection. By recording the coincidence rates for different polarization projections, we obtained the SWAP gate's truth table.

We first measured the logical operation of our PC-NOT gate by selecting an individual PC-NOT gate located on the same chip as our SWAP gate, with the same parameters as the SWAP gate's PC-NOTs. The characterization was performed using the measurement scheme shown in Fig. 2a (I). Figure 2b shows the resulting measured truth table obtained for the four input states $|00\rangle$, $|01\rangle$, $|10\rangle$ and $|11\rangle$ in the computational basis. The solid bars depict the experimentally measured truth table M_{exp} and the transparent bars illustrate the ideal truth table M_{ideal} . The fidelity of the measured PC-NOT truth table with respect to the ideal one is calculated by $F = (1/4) \text{Tr} \left(\frac{M_{\text{exp}} M_{\text{ideal}}^T}{M_{\text{ideal}} M_{\text{ideal}}^T} \right)$. In our PC-NOT gate,

we achieved an average fidelity of $97.8 \pm 0.3\%$ across the four basis states. We note that the residual deviation from unit fidelity is bounded by the PC-NOT's finite polarization extinction ratio (detailed in Supplementary Sections I and II) and the ~ 0.9 dB coupling difference between the $|H\rangle$ and $|V\rangle$ states. Similarly, to characterize our MC-NOT gate, we measured an individual polarization rotator located on the same chip, with the same parameters as the SWAP gate's MC-NOT. The test polarization rotator only has one spatial mode (Fig. 2c, top inset), so the truth table was only measured for two input polarization states: $|0\rangle$ and $|1\rangle$. The fidelity of the measured truth table in Fig. 2c with respect to the ideal one was $98.0 \pm 0.2\%$. We can infer the good performance of our on-chip MC-NOT gate, which is effectively a two-channel scheme of the polarization rotator and a silicon waveguide.

Having demonstrated the good performance of each individual gate in the logical basis, we next measured the truth table of our on-chip SWAP gate. The truth table was measured by four measurements, each for four input states. We recorded a total of $\sim 100,000$ coincidence counts in 160 s for the truth-table measurements, yielding a

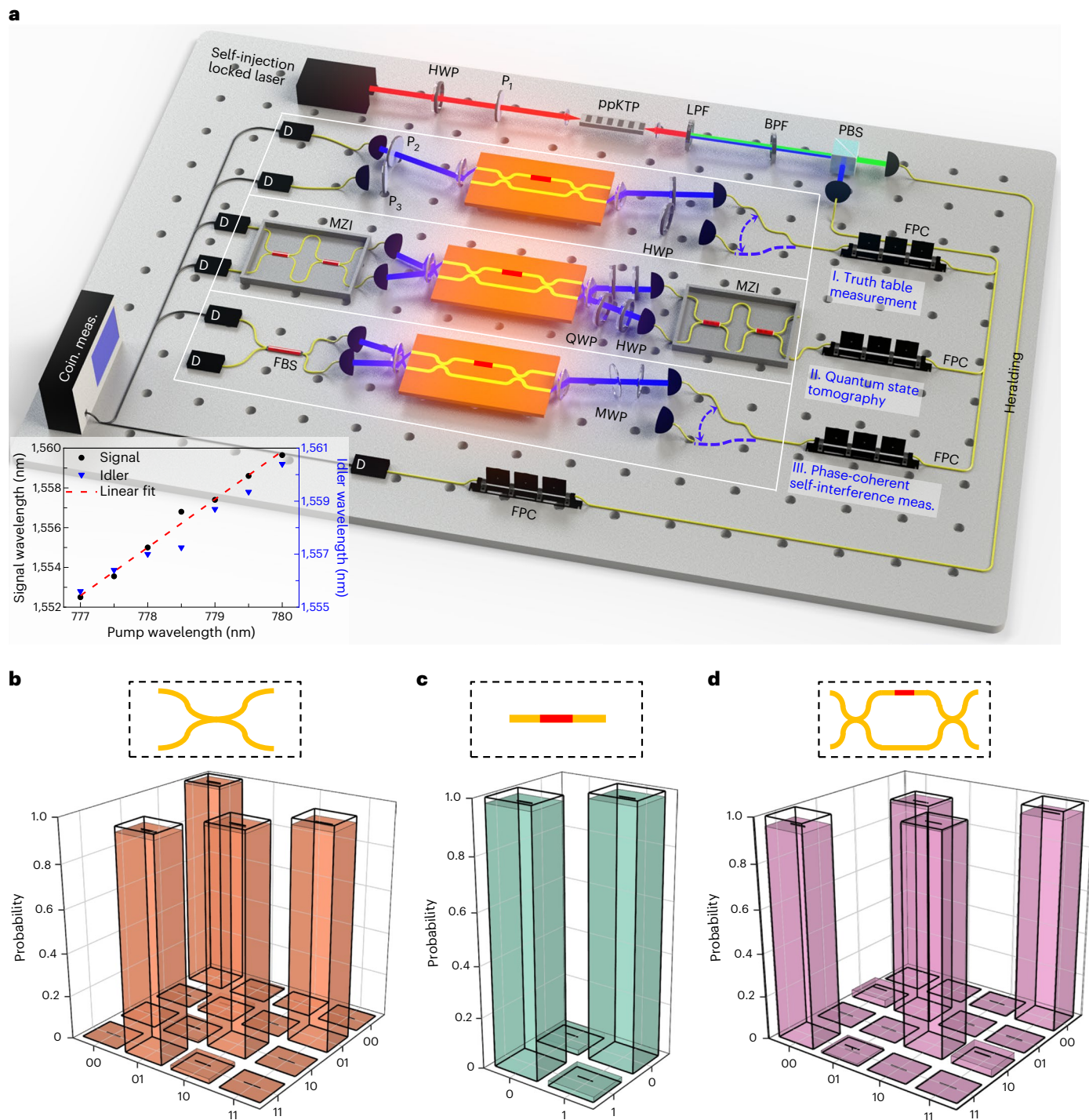
truth-table fidelity of $97.4 \pm 0.2\%$ at 1,557 nm, supporting the excellent performance in the logical basis. Truth-table measurements were also performed at 1,556 nm and 1,558 nm with similar fidelity (details are provided in Supplementary Section V), consistent with the broadband performance of the classical characterization. We attribute the deviations from unity in the truth-table fidelity mainly to the imperfect extinction ratio of the PC-NOT and MC-NOT gates and the MC-NOT gate's unbalanced photon loss.

Quantum state and process tomographies for the on-chip SWAP gate

Although the truth table measures the two-qubit SWAP operation in the logical basis, quantum process tomography is required to completely characterize the Hilbert space of the SWAP gate operation^{30,37}. First, we used bulk optics to prepare the signal photons in an input set of six polarization states $\rho_{\text{pol}}(|H\rangle, |V\rangle, |D\rangle, |A\rangle, |R\rangle, |L\rangle)$, as detailed in Supplementary Section VI, which were applied individually to the spatial input channels to the SWAP gate. Measuring the corresponding output spatial-momentum states ρ_{sm} provided the quantum state tomography for these polarization inputs. The six input polarizations are shown in the centre of Fig. 3a as Bloch vectors, and the reconstructed density matrices for each polarization state are provided in Supplementary Section VI. Two customized Mach–Zehnder interferometers (MZIs) with an extinction ratio of over 20 dB and two tunable delay lines were used to adjust the input spatial-momentum modes for the on-chip SWAP gate and project the output qubit on a set of six spatial-momentum states after the SWAP operation, respectively, with the measurement set-up shown in Fig. 2a (experiment II). The output spatial-momentum states were then analysed to perform quantum state tomography, with coincidence counts collected from the two output ports of the MZI. Bloch-sphere representations of the measured output spatial-momentum states are shown in Fig. 3a. The state fidelity is defined as $F = (\text{Tr}(\sqrt{\sqrt{\rho_{\text{pol}}}\rho_{\text{sm}}\sqrt{\rho_{\text{pol}}}}))^2$, which describes the overlap between the input polarization states and the measured output spatial-momentum states. For different spatial inputs, we achieved an averaged fidelity $\bar{F}_{\text{QST},T}$ of $97.2 \pm 0.3\%$ for the $|T\rangle$ input, $\bar{F}_{\text{QST},B}$ of $97.4 \pm 0.3\%$ for the $|B\rangle$ input, $\bar{F}_{\text{QST},+}$ of $97.1 \pm 0.2\%$ for the $|+\rangle$ input and $\bar{F}_{\text{QST},+i}$ of $97.0 \pm 0.1\%$ for the $|+i\rangle$ input. Reconstructed density matrix results for each spatial input are given in Supplementary Section VI. These high-fidelity output spatial-momentum states, with an average fidelity of $97.3 \pm 0.3\%$, confirm the successful single-qubit conversion from polarization qubit to spatial-momentum qubit.

Figure 3b shows the resulting process matrices of our SWAP gate for different spatial inputs. This SWAP gate operation process can be represented by a reconstructed process matrix χ , defined as $\rho_{\text{sm}} = \sum_{mn} \chi E_m \rho_{\text{pol}} E_n^\dagger$, where $E_{m(n)}$ are the identity I and Pauli matrices X , Y and Z , respectively. Thus, the SWAP gate's process matrix can be experimentally reconstructed by quantum state tomography (Fig. 3a). The process fidelity is defined as $F_\chi = \frac{\text{Tr}(\chi \chi_i)}{\text{Tr}(\chi) \text{Tr}(\chi_i)}$, where χ_i is the theoretically ideal process matrix. The X , Y and Z components of matrix χ represent the probability of bit-flip or phase-flip errors in the SWAP operation. We also evaluate the purity of the SWAP process matrix χ , defined as $P_\chi = \frac{\text{Tr}(\chi^2)}{\text{Tr}^2(\chi)}$, which is unity for an ideal process. Our SWAP gate is found to achieve a quantum process fidelity $\bar{F}_{\chi,T}$ of $95.5 \pm 0.2\%$ with a process purity of $91.6 \pm 0.2\%$ for the $|T\rangle$ spatial-momentum mode input, $\bar{F}_{\chi,B}$ of $95.3 \pm 0.2\%$ with a process purity of $91.6 \pm 0.6\%$ for the $|B\rangle$ input, $\bar{F}_{\chi,+}$ of $95.6 \pm 0.2\%$ with a process purity of $91.5 \pm 0.2\%$ for the $|+\rangle$ input, and $\bar{F}_{\chi,+i}$ of $95.4 \pm 0.1\%$ with a process purity of $91.2 \pm 0.3\%$ for the $|+i\rangle$ input. The average process fidelity for all spatial-momentum input modes is $95.5 \pm 0.1\%$, verifying the single-qubit SWAP operation of our silicon gate from polarization to spatial-momentum DoF.

For complete characterization of the two-qubit SWAP operation of our gate, we performed the full quantum process tomography.



heralding channel. P, linear polarizer; LPF, long-pass filter; BPF, band-pass filter; PBS, polarization beamsplitter; FPC, fibre polarization controller; MWP, multi-order waveplate; QWP, quarter-wave plate; MZI, Mach-Zehnder interferometer; FBS, 50:50 fibre beamsplitter; D, superconducting nanowire single-photon detector. Bottom left inset: signal and idler photon wavelengths as a function of the pump wavelength. The red dashed line is a linear fit on the signal-photon wavelength. **b–d**, Measured (solid bars) and ideal (transparent bars) truth table for the PC-NOT gate (**b**), MC-NOT gate (**c**) and SWAP gate (**d**) in the computational basis. A total of about 100,000 coincidence counts are recorded in 160 s for each measurement, yielding an average fidelity of $97.8 \pm 0.3\%$, $98.0 \pm 0.2\%$ and $97.4 \pm 0.2\%$, respectively.

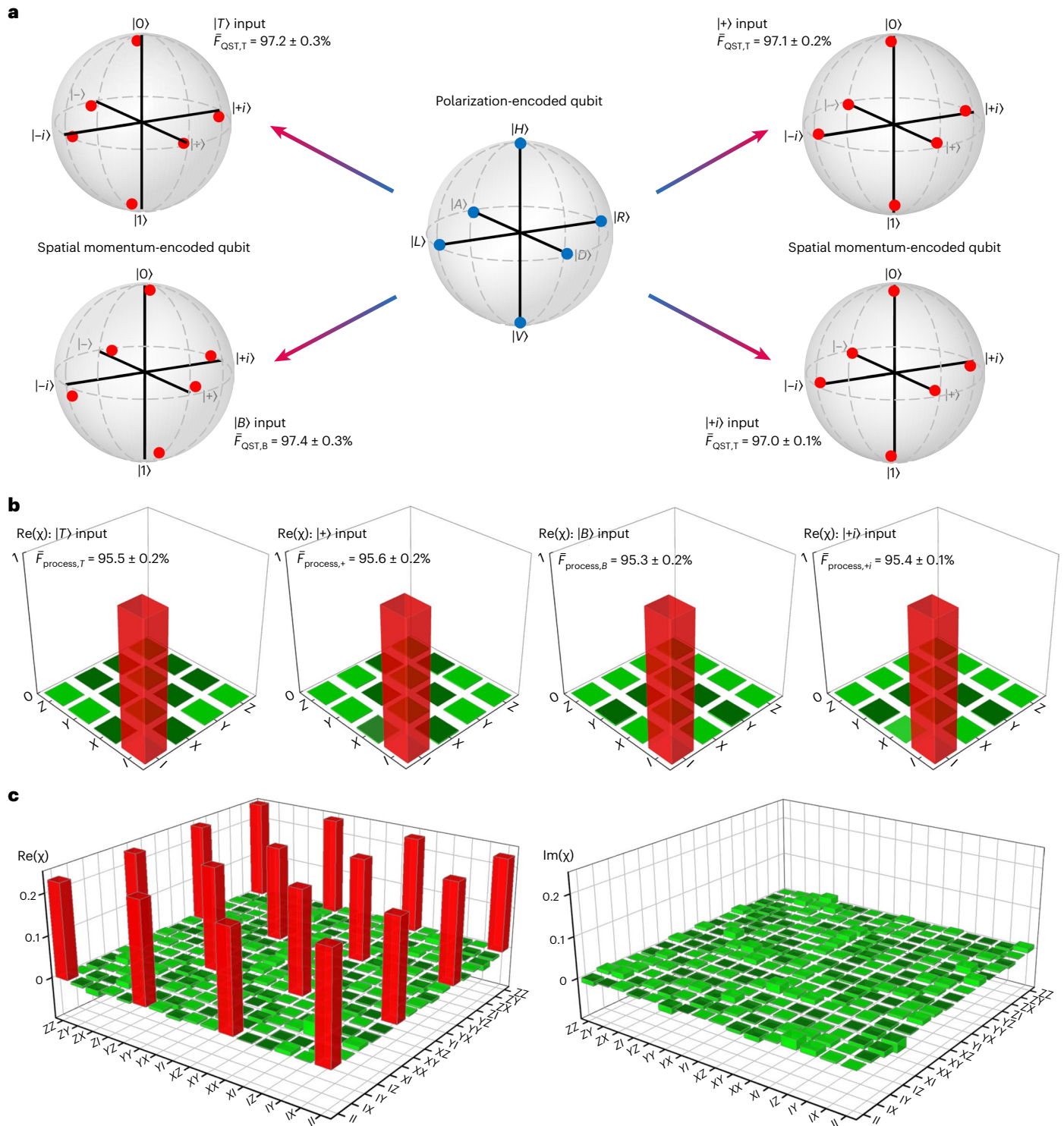


Fig. 3 | Quantum state and process tomographies for one-qubit and two-qubit SWAP operation. a, Output spatial-momentum-encoded states $|0\rangle, |1\rangle, |+\rangle, |-\rangle, |+\rangle$ and $|-\rangle$ measured by an MZI, represented by red dots on the Bloch sphere for input polarization qubits prepared in $|T\rangle, |B\rangle, |+\rangle$ and $|+\rangle$ spatial-momentum modes. The indicated fidelities represent averages over the six measured states. Middle: Bloch-sphere representation of six polarization-encoded input states $|H\rangle, |V\rangle, |D\rangle, |A\rangle, |R\rangle$ and $|L\rangle$, prepared by bulk optics (blue dots). **b**, Real parts of the reconstructed single-qubit process matrix χ of the SWAP gate for $|T\rangle, |B\rangle, |+\rangle$ and $|+\rangle$ spatial-momentum mode inputs, with an average process fidelity

of $95.5 \pm 0.1\%$ and process purity of $91.5 \pm 0.2\%$. All imaginary elements of the process matrix are smaller than 0.05. **c**, Reconstructed process matrix χ of the single-photon two-qubit SWAP gate. Additional to Fig. 2a (II), HWPs, QWPs and polarizers are inserted before the MZI at the chip output for polarization qubit analysis. Quantum state tomography (QST) results of the 16 input two-qubit states are presented in Supplementary Section VI, with an averaged state fidelity of $96.1 \pm 0.8\%$. The two-qubit SWAP process fidelity is measured to be $94.9 \pm 0.2\%$ with a process purity of $93.3 \pm 1.0\%$.

Additional to the process tomography measurement for single-qubit operation shown in Fig. 2a (II), waveplates and polarizers are inserted before the MZI at the output of the chip for the polarization qubit analysis. First, we prepared 16 separable, linearly independent states $\rho_{\text{sm, pol}} = |i_{\text{sm}} j_{\text{pol}}\rangle$ as input two-qubit states, where $i_{\text{sm}} = 0, 1, +, +i$ and $j_{\text{pol}} = H, V, D, R$. The output states are projected in the same 16-state basis $\{|i_{\text{sm}} j_{\text{pol}}\rangle\}$. The density matrix of the output states was reconstructed via quantum state tomography, with the results shown in Supplementary Section VI. An averaged state fidelity of $96.1 \pm 0.8\%$ is achieved for the 16 input states. The process matrix χ was then reconstructed in a similar manner as for the single-qubit tomography using a block matrix of the measured density matrices (Fig. 3c; details are provided in the Methods)³⁸. We achieved a process fidelity of $94.9 \pm 2.0\%$ with a process purity of $93.3 \pm 1.0\%$, which demonstrates the on-chip two-qubit SWAP operation of our gate. In addition, we note the sources of process fidelity non-ideality come from the bulk-optics imperfections in generating the input polarizations, the differential propagation loss and coupling efficiency mismatch between the $|H\rangle$ and $|V\rangle$ states, and the residual misalignment of the spatial mode projection in the MZI.

Quantum coherence of the on-chip SWAP operation

An ideal SWAP operation is a coherent phase-preserving process. For a polarization input state of the form $|H\rangle + e^{i\varphi}|V\rangle$, the output state can be written as $|T\rangle + e^{i(\varphi + \delta)}|B\rangle$, where the phase difference φ between the orthogonal polarizations is transferred to the spatial modes and a constant phase δ accounts for the path-length difference between the $|T\rangle$ and $|B\rangle$ spatial-momentum modes at the output. The $|T\rangle$ and $|B\rangle$ SWAP outputs of the signal photon are combined with a 50:50 fibre beamsplitter (FBS), as shown in Fig. 2a (III), the outputs of which are detected in coincidence with the heralding idler photon to yield a self-interference measurement of the signal photon as a function of φ . An adjustable path delay ΔT (not illustrated in the schematic) is included in the bottom channel of the SWAP output for balancing the lengths of the two interferometer arms.

In our measurements we start with a 45° linearly polarized qubit $|D\rangle$, and the phase shift φ is introduced via a tuned pair of MWPs (illustrated in Fig. 2a (III)) with their optical axes aligned to the $|V\rangle$ polarization. They are mounted on two motorized rotation stages for simultaneous counter-rotation along their optical axes. A tunable phase delay φ is imposed between $|H\rangle$ and $|V\rangle$ at the input by applying a rotation θ to one waveplate, while the transverse displacement of the beam is cancelled with the counter-rotation with the same angle magnitude for the other waveplate. The SWAP gate chip and the interference paths are carefully isolated from environmental noise for the phase-sensitive measurements. By sweeping the relative phase φ between the $|H\rangle$ and $|V\rangle$ polarizations of the input state of the signal photon, we can probe the phase coherence of our SWAP gate operation by self-interference between the $|T\rangle$ and $|B\rangle$ output spatial-momentum states.

Figure 4a shows the self-interference fringes of the two spatial-momentum modes of the signal photon after the SWAP operation at different wavelengths. For the $|T\rangle$ spatial-momentum input state, a raw fringe visibility of $98.7 \pm 0.2\%$ is obtained (99.4% after background subtraction) at $1,556 \text{ nm}$. This interference can also be observed when the polarization qubit is input through the bottom channel, with a raw visibility of $98.0 \pm 0.2\%$ (98.5% after background subtraction). The phase coherent polarization-to-spatial-momentum SWAP operation was also verified at $1,557 \text{ nm}$ and $1,558 \text{ nm}$ with high-visibility fringes, as shown in Fig. 4a, obtaining a wavelength-averaged single-photon self-interference visibility of $98.7 \pm 0.4\%$. These observed high-visibility fringes demonstrate successful phase-coherence transfer from the input's polarization qubit to the output's spatial-momentum qubit. Moreover, we note that the phase interference is long-term robust and can maintain high visibility up to $96.6 \pm 0.3\%$ over 24 h in free-running

operation without feedback stabilization (details are provided in Supplementary Section VII), verifying phase-stable implementation of the on-chip single-photon two-qubit SWAP gate.

The coherence-preserved SWAP operation for two photons was further verified by off-chip Hong–Ou–Mandel (HOM) interference^{39,40}, which measures the indistinguishability of the two photons over all DoFs. Implementing the experimental set-up in Fig. 2a (I), both signal and idler photons are fed to the on-chip SWAP gate via the two-in-two-out coupling system, using HWPs to control the input polarization. At the output end, instead of the polarizers, the two output channels are connected to a HOM interferometer consisting of a 50:50 FBS and a delay line. A fibre polarization controller on one arm of the HOM interferometer ensures that the polarization of the two output photons will be the same at the FBS. By tuning the delay line, we can sweep the arrival time difference between the two output photons at the FBS and obtain the HOM interference dip. Figure 4b shows the measured HOM interference between the two output photons for different input polarization combinations. For the $|T_S V_S\rangle \otimes |B_I H_I\rangle$ input, a HOM visibility of $96.9 (92.4) \pm 1.4\%$ is obtained after (before) background subtraction. For the $|T_S H_S\rangle \otimes |B_I V_I\rangle$ input, a HOM visibility of $96.0 (91.0) \pm 1.9\%$ is achieved after (before) background subtraction. The slightly lower visibility for the $|T_S H_S\rangle \otimes |B_I V_I\rangle$ input is because both signal and idler photons propagate through the polarization rotator on the upper arm of the SWAP gate, which introduces extra loss compared to the case for the $|T_S V_S\rangle \otimes |B_I H_I\rangle$ input. The HOM dip width indicates the two-photon coherence time, which is measured to be $3.17 \pm 0.02 \text{ ps}$ for the $|T_S V_S\rangle \otimes |B_I H_I\rangle$ input and $3.11 \pm 0.03 \text{ ps}$ for the $|T_S H_S\rangle \otimes |B_I V_I\rangle$ input. The indistinguishability of the SPDC photon pairs was also examined using the same HOM interferometer (as detailed in Supplementary Section VIII), finding a HOM visibility of $97.9 (93.4) \pm 1.0\%$ after (before) background subtraction and a two-photon coherence time of $3.15 \pm 0.02 \text{ ps}$. The small deviation of the HOM interference visibility and two-photon coherence time after the SWAP operation compared to the SPDC source unambiguously proves the preservation of the quantum coherence in the on-chip SWAP gate process. The observed HOM interference dip also verifies the indistinguishability between the two output spatial modes of the on-chip SWAP gate, which is crucial for path-mode entanglement generation on chip, enabled by quantum interference^{41,42}.

Quantum state distribution between dual SWAP gate chips

With coherence-preserved SWAP gate operation verified with high fidelity on our silicon chip, we next demonstrate an efficient quantum photonic interconnect between different DoFs utilizing the reversible conversion of our on-chip SWAP process. The experimental scheme of the chip-to-chip interconnect is illustrated in Fig. 4c. The input two-qubit maximally entangled state φ is prepared in the polarization basis. Polarization Bell state $|\psi^+\rangle = (|HV\rangle + |VH\rangle)/\sqrt{2}$ is first generated by temporally overlapping the SPDC biphotons at a beamsplitter with orthogonal polarization (as detailed in the Methods)³⁶. The signal and idler photons are then fed to the $|T\rangle$ and $|B\rangle$ channels of the first SWAP gate chip, respectively. The input state can thus be written as $\varphi = (|H_S V_I\rangle + |V_S H_I\rangle) \otimes |T_S B_I\rangle/\sqrt{2}$. The first SWAP gate then deterministically swaps the entanglement from polarization to spatial-momentum, yielding $\varphi_{\text{sm}} = (|B_S T_I\rangle + |T_S B_I\rangle) \otimes |V_S H_I\rangle/\sqrt{2}$. The output spatial-momentum entangled state is transmitted to the second SWAP gate chip via a single-mode fibre link, where the polarization rotation during transmission is compensated by the QWPs and HWPs at the input of the second chip. The second SWAP gate has the same structural parameters as the first SWAP gate, and is characterized with a truth table $\bar{F}_{\text{gate, truth}}$ of $97.2 \pm 0.3\%$ (details are provided in Supplementary Section IX). The spatial-momentum entangled state is then reversibly converted to polarization entangled state φ by the second SWAP gate, and measured by polarization analysers consisting of a QWP, HWP and polarizer to perform quantum state tomography.

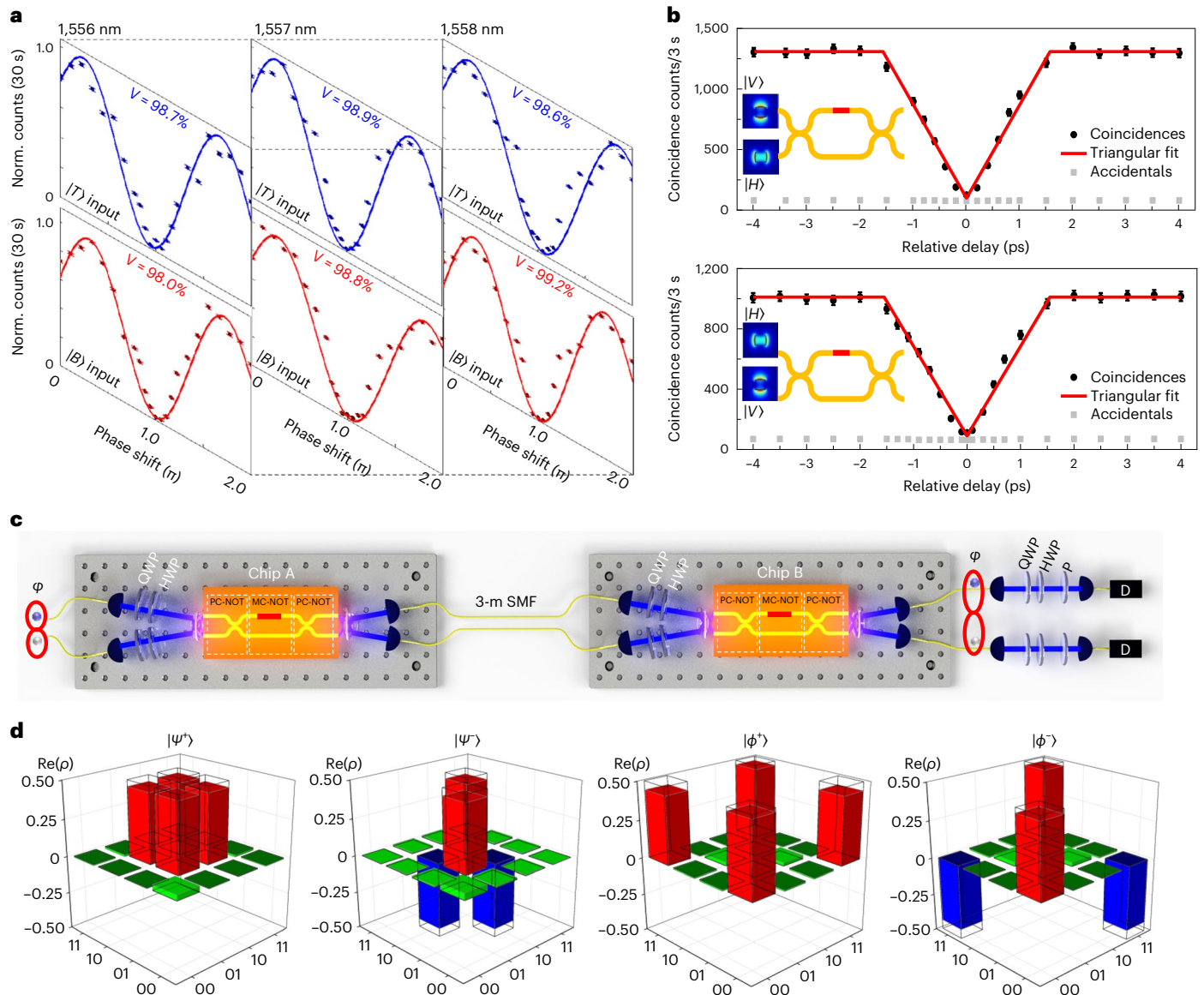


Fig. 4 | Coherence preservation of the SWAP gate and quantum state distribution between dual SWAP gate chips. a, A polarization qubit $|H\rangle + e^{i\phi}|V\rangle$ is sent to the SWAP gate to probe the phase coherence of the single-photon two-qubit SWAP operation. Interference fringes are obtained by tuning the phase shift ϕ with a pair of MWPs (illustrated in Fig. 2a (III)), while collecting coincidence counts between signal and idler photons (accumulated for 30 s). Measured at 1,556 nm, 1,557 nm and 1,558 nm, the phase interference has fringe visibilities of $98.7 (99.4) \pm 0.2\%$, $98.9 (99.3) \pm 0.2\%$ and $98.6 (98.9) \pm 0.2\%$, respectively, for the $|T\rangle$ input state before (after) background subtraction. For the $|B\rangle$ input state, the fringe visibilities are $98.0 (98.5) \pm 0.2\%$, $98.8 (99.0) \pm 0.2\%$ and $99.2 (99.4) \pm 0.1\%$, respectively, before (after) background subtraction. **b**, Hong–Ou–Mandel interference between two photons after the SWAP operation for different input polarization combinations. A visibility of $96.9 (92.4) \pm 1.4\%$ is achieved for the $|T_S V_S\rangle \otimes |B_I H_I\rangle$ input and $96.0 (91.0) \pm 1.9\%$ for the $|T_S H_S\rangle \otimes |B_I V_I\rangle$ input after (before) background subtraction, which proves the preservation of quantum coherence after the on-chip SWAP operation. Data are presented as mean

values \pm s.d. with $n = 3$. Error bars are calculated from three sets of measurements assuming Poissonian statistics. **c**, Experimental scheme for the quantum state distribution between two silicon SWAP gate chips. Polarization Bell states are prepared and fed into the first on-chip SWAP gate; then the swapped spatial-momentum states are transmitted through 3 m of single-mode fibre (SMF) and coupled to the second on-chip SWAP gate (the truth-table measurement is provided in Supplementary Section IX), which converts the spatial-momentum states back to the polarization states. Polarization analysers, consisting of a QWP, HWP and polarizer, measure the polarization entangled states after the second on-chip SWAP gate for tomographic characterization. **d**, Real parts of the reconstructed density matrices of the polarization Bell states $|\Psi^+\rangle$, $|\Psi^-\rangle$, $|\Phi^+\rangle$ and $|\Phi^-\rangle$, with an averaged Bell-state fidelity of $91.5 \pm 0.8\%$ after the chip-to-chip distribution, verifying the coherent reversible conversion of the SWAP operation between two silicon chips. The imaginary parts of the density matrices are negligible.

By adjusting the HWPs and QWPs at the input of the first SWAP gate, the other three Bell states $|\Psi^-\rangle$, $|\Phi^+\rangle$ and $|\Phi^-\rangle$ can be produced for chip-to-chip distribution⁴³.

Figure 4d shows the experimentally reconstructed density matrices for four polarization Bell states. The state fidelity is calculated by

$$F_{\text{Bell}} = (\text{Tr}(\sqrt{\sqrt{\rho_{\text{Ideal}}}\rho_{\text{Bell}}\sqrt{\rho_{\text{Ideal}}}}))^2$$

which describes the overlap between

the ideal Bell states and the measured states. The fidelities of the reconstructed density matrices compared to the corresponding Bell states are $F_{|\Psi^+\rangle} = 92.5 \pm 0.3\%$, $F_{|\Psi^-\rangle} = 90.4 \pm 0.5\%$, $F_{|\Phi^+\rangle} = 92.0 \pm 0.6\%$ and $F_{|\Phi^-\rangle} = 91.1 \pm 0.7\%$, with an averaged fidelity of $91.5 \pm 0.8\%$. The non-ideality of the fidelity is attributed to the waveguide loss, unbalanced coupling efficiency, imperfect rotation of the polarization elements and misalignment of the polarization analysers.

The chip-to-chip distribution of the four Bell states demonstrates the coherent reversible conversion of our SWAP gate between polarization and spatial-momentum DoF. This demonstration also provides a practical tool for the quantum interconnect of distant photonic platforms with different DoFs towards achieving distributed quantum computation and quantum sensing^{17,44}.

Discussion

We have successfully demonstrated a deterministic single-photon two-qubit SWAP gate between polarization and spatial-momentum on a silicon chip. The performance of our on-chip SWAP gate can be further improved by optimizing the fabrication parameters and chip coupling. We note that the deviations from unity in the truth-table fidelity mainly arise from the imperfect extinction ratio of the PC-NOT and MC-NOT gates and the MC-NOT gate's unbalanced photon loss. These non-idealities are examined in detail in Supplementary Section X and can be mitigated by more adiabatic polarization-mode conversion and tighter suppression of the cross-polarization. In addition, we note that the waveguide loss and unbalanced coupling efficiency between the $|H\rangle$ and $|V\rangle$ states contribute to a truth-table fidelity reduction by $\sim 0.5\%$. With recent progress on integrated polarization devices, PBSs with extinction ratios of over 35 dB and polarization rotators with low insertion loss have been realized on a silicon platform³², which can bring our chip's truth-table fidelity up to near-unity. In addition, a silicon-based MZI with an extinction ratio of over 66 dB has been achieved, which will further improve the path-mode projection for quantum state tomography measurements⁴⁵.

The quantum coherence is preserved during the on-chip SWAP process, and the coherent reversible conversion enables quantum interconnectivity between two chips. We note that conversion of photonic quantum states between different DoFs has been demonstrated on chip^{40,46}, but none have demonstrated an on-chip two-qubit SWAP gate operation. With the CMOS-compatible silicon chip-scale platform, high-density photonic integration involving different DoFs might be possible for future applications⁴⁷, extending to high-dimensional quantum gate operation^{48,49}, with intrinsic good phase stability and compactness. The demonstrated quantum photonic interconnect can facilitate applications exploiting polarization and spatial-momentum entanglement between chip-based subsystems. In addition, the compatibility with microelectronics enables monolithic integration of photon sources, logic circuits and detectors on a silicon platform^{20,50}. Our on-chip SWAP gate paves the way for deterministic chip-scale quantum information processing and provides a photonic quantum interface for interconnected quantum information systems towards achieving a quantum internet.

Online content

Any methods, additional references, Nature Portfolio reporting summaries, source data, extended data, supplementary information, acknowledgements, peer review information; details of author contributions and competing interests; and statements of data and code availability are available at <https://doi.org/10.1038/s41566-023-01224-x>.

References

- Harrow, A. W. & Montanaro, A. Quantum computational supremacy. *Nature* **549**, 203–209 (2017).
- Preskill, J. Quantum computing in the NISQ era and beyond. *Quantum* **2**, 79 (2018).
- Arute, F. et al. Quantum supremacy using a programmable superconducting processor. *Nature* **574**, 505–510 (2019).
- Zhong, H.-S. et al. Quantum computational advantage using photons. *Science* **370**, 1460–1463 (2020).
- O'Brien, J. L. Optical quantum computing. *Science* **318**, 1567–1570 (2007).
- Knill, E., Laflamme, R. & Milburn, G. J. A scheme for efficient quantum computation with linear optics. *Nature* **409**, 46–52 (2001).
- Wang, X.-L. et al. 18-Qubit entanglement with six photons' three degrees of freedom. *Phys. Rev. Lett.* **120**, 260502 (2018).
- Kok, P. et al. Linear optical quantum computing with photonic qubits. *Rev. Mod. Phys.* **79**, 135–174 (2007).
- Raussendorf, R. & Briegel, H. J. A one-way quantum computer. *Phys. Rev. Lett.* **86**, 5188–5191 (2001).
- Walther, P. et al. Experimental one-way quantum computing. *Nature* **434**, 169–176 (2005).
- O'Brien, J., Furusawa, A. & Vučković, J. Photonic quantum technologies. *Nat. Photon.* **3**, 687–695 (2009).
- Fiorentino, M. & Wong, F. N. C. Deterministic controlled-NOT gate for single-photon two-qubit quantum logic. *Phys. Rev. Lett.* **93**, 070502 (2004).
- Carolan, J. et al. Universal linear optics. *Science* **349**, 711–716 (2015).
- Kimble, H. J. The quantum internet. *Nature* **453**, 1023–1030 (2008).
- Wehner, S., Elkouss, D. & Hanson, R. Quantum internet: a vision for the road ahead. *Science* **362**, eaam9288 (2018).
- Cacciapuoti, A. S. et al. Quantum internet: networking challenges in distributed quantum computing. *IEEE Netw.* **34**, 137–143 (2020).
- Awschalom, D. et al. Development of quantum interconnects for next-generation information technologies. *PRX Quantum* **2**, 017002 (2021).
- Erhard, M., Krenn, M. & Zeilinger, A. Advances in high-dimensional quantum entanglement. *Nat. Rev. Phys.* **2**, 365–381 (2020).
- Wang, J., Sciarrino, F., Laing, A. & Thompson, M. G. Integrated photonic quantum technologies. *Nat. Photon.* **14**, 273–284 (2020).
- Wang, J. et al. Multidimensional quantum entanglement with large-scale integrated optics. *Science* **360**, 285–291 (2018).
- Qiang, X. et al. Large-scale silicon quantum photonics implementing arbitrary two-qubit processing. *Nat. Photon.* **12**, 534–539 (2018).
- Barz, S. et al. Demonstration of blind quantum computing. *Science* **335**, 303–308 (2012).
- Cirac, J. I., Ekert, A. K., Huelga, S. F. & Macchiavello, C. Distributed quantum computation over noisy channels. *Phys. Rev. A* **59**, 4249–4254 (1999).
- Sheng, Y.-B. & Zhou, L. Distributed secure quantum machine learning. *Sci. Bull.* **62**, 1025–1029 (2017).
- Fiorentino, M., Kim, T. & Wong, F. N. C. Single-photon two-qubit SWAP gate for entanglement manipulation. *Phys. Rev. A* **72**, 012318 (2005).
- Kagalwala, K. H., Di Giuseppe, G., Abouraddy, A. F. & Saleh, B. E. A. Single-photon three-qubit quantum logic using spatial light modulators. *Nat. Commun.* **8**, 739 (2017).
- Lu, H.-H. et al. Quantum phase estimation with time-frequency qudits in a single photon. *Adv. Quantum Tech.* **3**, 1900074 (2020).
- Zhang, M. et al. Supercompact photonic quantum logic gate on a silicon chip. *Phys. Rev. Lett.* **126**, 130501 (2021).
- Li, J.-P. et al. Heralded nondestructive quantum entangling gate with single-photon sources. *Phys. Rev. Lett.* **126**, 140501 (2021).
- Nielsen, M. A. & Chuang, I. L. *Quantum Computation and Quantum Information* (Cambridge Univ. Press, 2000).
- Barwicz, T. et al. Polarization-transparent microphotonic devices in the strong confinement limit. *Nat. Photon.* **1**, 57–60 (2007).
- Su, Y., Zhang, Y., Qiu, C., Guo, X. & Sun, L. Silicon photonic platform for passive waveguide devices: materials, fabrication and applications. *Adv. Mater. Technol.* **5**, 1901153 (2020).
- Goi, K. et al. Low-loss partial rib polarization rotator consisting only of silicon core and silica cladding. *Opt. Lett.* **40**, 1410–1413 (2015).

34. Horikawa, T. et al. A 300-mm silicon photonics platform for large-scale device integration. *IEEE J. Sel. Top. Quantum Electron.* **24**, 8200415 (2018).
35. Chang, K.-C. et al. 648 Hilbert space dimensionality in a biphoton frequency comb: entanglement of formation and Schmidt mode decomposition. *NPJ Quantum Inf.* **7**, 48 (2021).
36. Xie, Z. et al. Harnessing high-dimensional hyperentanglement through a biphoton frequency comb. *Nat. Photon.* **9**, 536–542 (2015).
37. O'Brien, J. L. et al. Quantum process tomography of a controlled-NOT gate. *Phys. Rev. Lett.* **93**, 080502 (2004).
38. White, A. G. et al. Measuring two-qubit gates. *J. Opt. Soc. Am. B* **24**, 172–183 (2007).
39. Hong, C. K., Ou, Z. Y. & Mandel, L. Measurement of subpicosecond time intervals between two photons by interference. *Phys. Rev. Lett.* **59**, 2044–2046 (1987).
40. Feng, L.-T. et al. On-chip coherent conversion of photonic quantum entanglement between different degrees of freedom. *Nat. Commun.* **7**, 11985 (2016).
41. Silverstone, J. W. et al. On-chip quantum interference between silicon photon-pair sources. *Nat. Photon.* **8**, 104–108 (2014).
42. Llewellyn, D. et al. Chip-to-chip quantum teleportation and multi-photon entanglement in silicon. *Nat. Phys.* **16**, 148–153 (2020).
43. Kwiat, P. G. et al. New high-intensity source of polarization-entangled photon pairs. *Phys. Rev. Lett.* **75**, 4337–4341 (1995).
44. Zhang, Z. & Zhuang, Q. Distributed quantum sensing. *Quantum Sci. Technol.* **6**, 043001 (2021).
45. Harris, N. C. et al. Quantum transport simulations in a programmable nanophotonic processor. *Nat. Photon.* **11**, 447–452 (2017).
46. Wang, J. et al. Chip-to-chip quantum photonic interconnect by path-polarization interconversion. *Optica* **3**, 407–413 (2016).
47. Xiong, C. et al. Compact and reconfigurable silicon nitride time-bin entanglement circuit. *Optica* **2**, 724–727 (2015).
48. Gao, X., Erhard, M., Zeilinger, A. & Krenn, M. Computer-inspired concept for high-dimensional multipartite quantum gates. *Phys. Rev. Lett.* **125**, 050501 (2020).
49. Imany, P. et al. High-dimensional optical quantum logic in large operational spaces. *NPJ Quantum Inf.* **5**, 59 (2019).
50. Najafi, F. et al. On-chip detection of non-classical light by scalable integration of single-photon detectors. *Nat. Commun.* **6**, 5873 (2015).

Publisher's note Springer Nature remains neutral with regard to jurisdictional claims in published maps and institutional affiliations.

Springer Nature or its licensor (e.g. a society or other partner) holds exclusive rights to this article under a publishing agreement with the author(s) or other rightsholder(s); author self-archiving of the accepted manuscript version of this article is solely governed by the terms of such publishing agreement and applicable law.

© The Author(s), under exclusive licence to Springer Nature Limited 2023

Methods

Chip fabrication

Our on-chip SWAP gate consists of two PC-NOT gates and an MC-NOT gate. The PC-NOT gate is a silicon waveguide device realized by a polarized directional coupler. The silicon MC-NOT gate is realized by a specially designed two-layer polarization rotator that consists of a polarization rotation stage with an asymmetric partial-rib waveguide and a polarization-maintaining mode conversion stage with a nano-tapered waveguide. With further detail provided in Supplementary Section I.B, the MC-NOT consists of three sections, with a middle-section slab height of 110 nm. The core width adiabatically evolves from 300-nm width at the gate input to 180-nm width at the middle-section interface region, and back to 300-nm width at the gate output. With the continuous mode evolution designed into our MC-NOT gate, the insertion losses are -0.5 dB and 1.0 dB for the TE-to-TM and TM-to-TE polarizations, respectively, while preserving a 20-dB extinction in the TE and TM polarizations. The designed gate is fabricated on a silicon-on-insulator wafer using a CMOS-based process with a KrF excimer laser stepper. The top silicon layer is 220 nm thick and the thickness of the buried oxide layer is 3 μm . The asymmetric partial rib of the core is formed by two-step dry-etching processes, specifically achieved by a developed self-aligned process for this study (detailed in Supplementary Section II). A 2- μm SiO₂ cladding is deposited on top of the core by high-density plasma-enhanced chemical vapour deposition. The total length of the polarization rotator is 360 μm . For photon input–output coupling, our standardized design library with inverse adiabatic couplers is implemented. This consists of a silicon nano-tip of -180 nm, with mode evolving to the standardized single-mode width. The SiO₂ cladding on the nano-tip forms an oxide waveguide, with air trenches on the lateral transverse sides of the oxide waveguide. Deep reactive ion etching forms the input and output facets. The complete SWAP gate (input–output couplers, PC-NOT and MC-NOT gates) only requires silicon and silicon-oxide interfaces, which are compatible with silicon foundries.

Quantum process tomography

A quantum operation can be completely determined by experimentally measuring the output quantum states from a set of pure input states³⁰. Any quantum process can be represented by a χ matrix, which is $2^{2N} \times 2^{2N}$ for an N -qubit operation. Such a χ matrix can be experimentally reconstructed by quantum process tomography³⁸. For a fixed set of operators \bar{E} , the output state after a quantum process for an input state ρ can be expressed in the operator sum representation as $\rho' = \sum_{m,n} \chi_{mn} \bar{E}_m \rho \bar{E}_n^\dagger$. For single-qubit process tomography of our on-chip SWAP gate, we selected the operator basis \bar{E} with four Pauli matrices $\sigma_x, \sigma_y, \sigma_z$ and I . We prepared four linearly independent polarization states $|H\rangle, |V\rangle, |D\rangle = (|H\rangle + |V\rangle)/\sqrt{2}$ and $|R\rangle = (|H\rangle + i|V\rangle)/\sqrt{2}$ as inputs, and measured the output states in the spatial-momentum basis $|0\rangle, |1\rangle, |+\rangle = (|0\rangle + |1\rangle)/\sqrt{2}$ and $|+\rangle = (|0\rangle + i|1\rangle)/\sqrt{2}$. The process matrix χ of the single-qubit SWAP operation is then expressed as $\chi = \Lambda \begin{pmatrix} \rho'_1 & \rho'_2 \\ \rho'_3 & \rho'_4 \end{pmatrix} \Lambda$, where the matrix ρ' is determined via quantum state tomography, and the block matrix Λ is defined as $\Lambda = \frac{1}{2} \begin{pmatrix} I & \sigma_x \\ \sigma_x & -I \end{pmatrix}$.

For two-qubit process tomography of our on-chip SWAP gate, we selected the operator basis $\bar{E} = \sigma_m \otimes \sigma_n$, where $m, n = I, X, Y, Z$. We prepared 16 linearly independent states $\rho_{\text{sm}, \text{pol}} = |i_{\text{sm}}, j_{\text{pol}}\rangle$ as input two-qubit states, where $i_{\text{sm}} = 0, 1, +, +i$ and $j_{\text{pol}} = H, V, D, R$. The output states were then measured in the same basis with density matrices reconstructed via quantum state tomography. The process matrix χ of the two-qubit SWAP operation can be reconstructed similarly using a block matrix of the measured density matrices by:

$$\chi = K^T \begin{pmatrix} \rho'_{11} & \rho'_{12} & \rho'_{13} & \rho'_{14} \\ \rho'_{21} & \rho'_{22} & \rho'_{23} & \rho'_{24} \\ \rho'_{31} & \rho'_{32} & \rho'_{33} & \rho'_{34} \\ \rho'_{41} & \rho'_{42} & \rho'_{43} & \rho'_{44} \end{pmatrix} K$$

Here, $K = P\Lambda$, $P = I \otimes [M \otimes I]$, $\Lambda = \frac{1}{4} (\sigma_z \otimes I + \sigma_x \otimes \sigma_x) \otimes (\sigma_z \otimes I + \sigma_x \otimes \sigma_x)$ and

$$M = \begin{pmatrix} 1 & 0 & 0 & 0 \\ 0 & 0 & 1 & 0 \\ 0 & 1 & 0 & 0 \\ 0 & 0 & 0 & 1 \end{pmatrix}$$

The reconstructed density matrices and process matrices may be nonphysical due to the noise in the measurement process, so we employ the maximum-likelihood estimation for both quantum state and process tomography to find the closest matrix to the measured one³⁸. The process fidelity is defined as $F_\chi = \frac{\text{Tr}(\chi\chi_i)}{\text{Tr}(\chi)\text{Tr}(\chi_i)}$ for both single-qubit and two-qubit process tomography, where χ_i is the theoretically ideal process matrix. The purity of the SWAP process (matrix χ) is also evaluated as $P_\chi = \frac{\text{Tr}(\chi^2)}{\text{Tr}^2(\chi)}$, which is unity for an ideal process.

Bell-state preparation

The polarization Bell states for the chip-to-chip distribution were prepared by post-selection. We first mixed the signal and idler photons on a 50:50 fibre coupler with orthogonal polarizations. To ensure good temporal overlapping between the signal and idler photons, we swept the relative delay between them to find the HOM dip (as detailed in Supplementary Section VIII) and then rotated the polarization of the signal photons by 90°. The post-selected polarization entanglement was verified after the fibre coupler via polarization projection measurements with $94.2 \pm 0.9\%$ fringe visibility, and $S = 2.664 \pm 0.029$ violating the classical limit by more than 22 s.d.^{35,36}. The two output ports of the 50:50 fibre coupler were then connected to the top and bottom channels of the first SWAP gate chip. We inserted a pair of a HWP and a QWP at the input of the first SWAP gate chip. The polarization Bell state $|\Psi^+\rangle$ can be tuned to $|\Phi^+\rangle$ by the HWP or to $|\Psi^-\rangle$ by the QWP in one input path. By appropriately orienting the waveplates, we were able to prepare four polarization Bell states for distribution between dual SWAP gate chips⁴³.

Data availability

All the data and methods are presented in the main text and the Supplementary Information. The figures are also available on Figshare at <https://doi.org/10.6084/m9.figshare.22590367>. The raw datasets generated and/or analysed during the current study are available from the corresponding author upon request. Source data are provided with this paper.

Acknowledgements

We acknowledge discussions with H. Liu, K. Yu, Y. Cho, A. Veitia, T. Zhong and F. Sun and SEM assistance from J. F. McMillan. This work is supported by the National Science Foundation (EFRI-ACQUIRE 1741707, QII-TAQS 1936375, 1919355 and 2008728) and the University of California National Laboratory research programme (LFRP-17-477237).

Author contributions

X.C., K.C.C., Z.X. and Y.S.L. performed the measurements. Y.L., S.K. and X.X. performed the design layout. M.Y., P.G.Q.L. and D.L.K. performed the device nanofabrication. X.C., M.C.S., X.X., A.K.V., J.H.S. and F.N.C.W. contributed to the theory and numerical modelling. X.C., Z.X., X.X., J.H.S., F.N.C.W. and C.W.W. wrote the manuscript, with contributions from all authors.

Competing interests

The authors declare no competing interests.

Additional information

Supplementary information The online version contains supplementary material available at <https://doi.org/10.1038/s41566-023-01224-x>.

Correspondence and requests for materials should be addressed to Xiang Cheng, Kai-Chi Chang or Chee Wei Wong.

Peer review information *Nature Photonics* thanks Marco Fiorentino and the other, anonymous, reviewer(s) for their contribution to the peer review of this work.

Reprints and permissions information is available at www.nature.com/reprints.

A chip-scale polarization-spatial-momentum quantum SWAP gate in silicon nanophotonics

In the format provided by the authors and unedited

This Supplementary Information consists of the below sections:

I. Design and operation maps of the two-qubit SWAP gate components: PC-NOT and MC-NOT gates

I.A. PC-NOT gate design and implementation

I.B. MC-NOT gate design and implementation

II. Nanofabrication and characterization of the PC-NOT and MC-NOT gates

II.A. Nanofabrication of the silicon MC-NOT gate

II.B. Characterization of the PC-NOT gate

II.C. Characterization of the MC-NOT gate

III. Spectral and broadband characterization of the on-chip SWAP gate

IV. Double-pass self-injection-locked pump laser

V. Truth table of SWAP gate at different wavelengths

VI. Quantum state tomography after SWAP gate operation

VI.A. Single-qubit quantum state tomography

VI.B. Two-qubit quantum state tomography

VII. Measured long-term stability of the single-photon self-interference after the SWAP operation

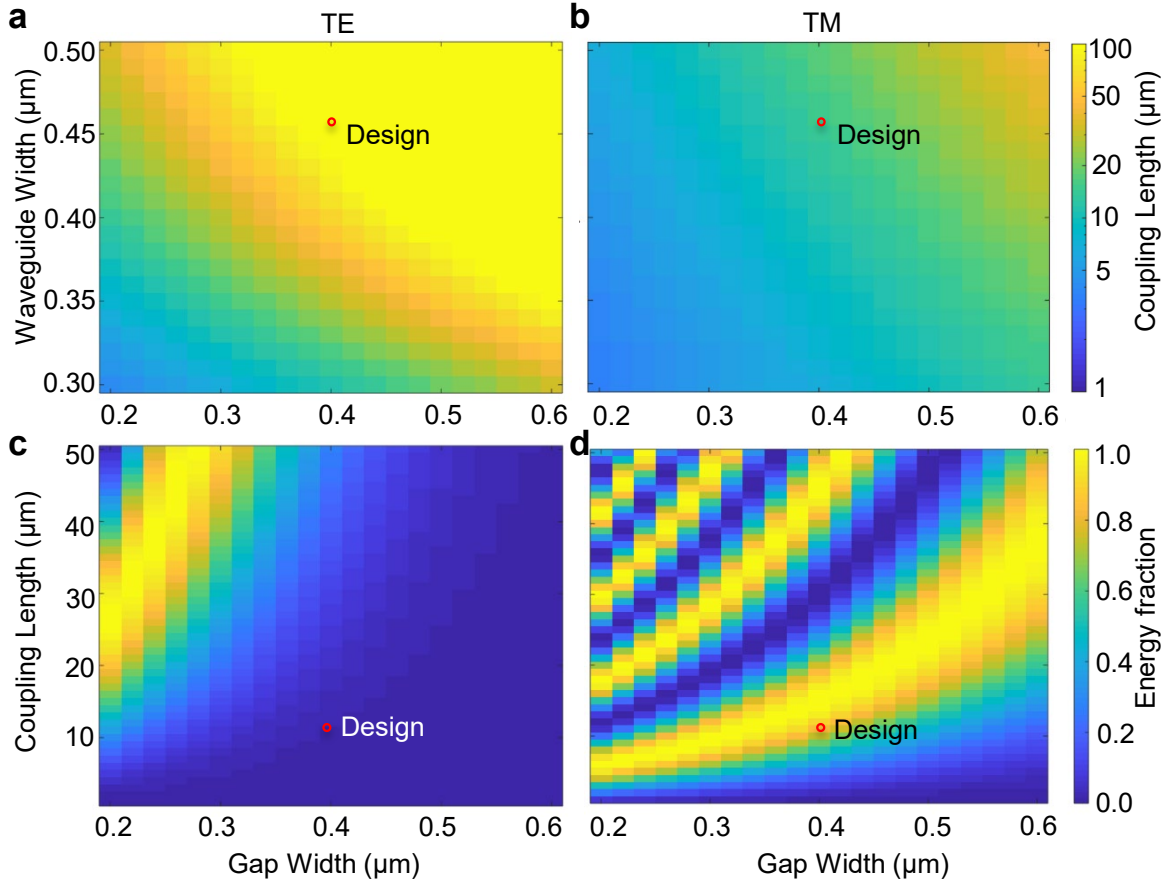
VIII. Hong-Ou-Mandel interference of the biphotons from the SPDC source

IX. Truth table measurement of the second on-chip SWAP gate

X. Impact of imbalanced photon loss and cross-polarization suppression on the SWAP gate fidelity

I. Design and operation maps for the two-qubit SWAP gate's PC-NOT and MC-NOT gates

I.A. PC-NOT gate design and implementation: SWAP gate is of special value in quantum circuit architectures, as it coherently transfers qubits in different degree-of-freedom without measuring or perturbing them, and thus serves as an ideal quantum interface [S1-S5]. Our SWAP gate consists of three successive controlled-NOT (C-NOT) operations, implemented with PC-NOT, MC-NOT, and PC-NOT cascade. To ensure our single-photon two-qubit SWAP gate's implementation provides high-quality performance, we made thorough individual design-space studies of the PC-NOT and MC-NOT gates. The design map for the PC-NOT gate was prepared with an eigenmode solver through super-mode analysis of the silicon polarized directional-coupler photonics structure as functions of waveguide and gap widths. The eigenmode results were verified through a detailed propagator analysis using the finite-difference time-domain (FDTD) method and a proper parameter set was selected for our PC-NOT implementation. Here, polarization splitting is satisfied by carefully selecting the coupler length to equal to the transverse magnetic (TM) coupling length, which is about ten times smaller than that for the transverse electric (TE) case. Varying gap widths, crossover coupling lengths and waveguide widths are illustrated for the optimal coupling length and cross-channel energy fraction in Supplementary Figure 1. The silicon waveguides were designed with 220 nm thickness for operation in the C-band. Supplementary Figure 1a and 1b show the coupling length for the given configurations. By fixing the waveguide width to 460 nm, the energy fractions coupled to the cross-channel were monitored for varying coupler lengths and gap widths, as shown in Supplementary Figure 1c and 1d. The optimized design for the PC-NOT gate has a waveguide-to-waveguide gap width of 400 nm and a coupling length of 11.5 μm . With this parameter combination, the TE mode remains in its channel while the TM mode crosses over to the other channel with maximized efficiency, thus ensuring optimal PC-NOT gate operation.

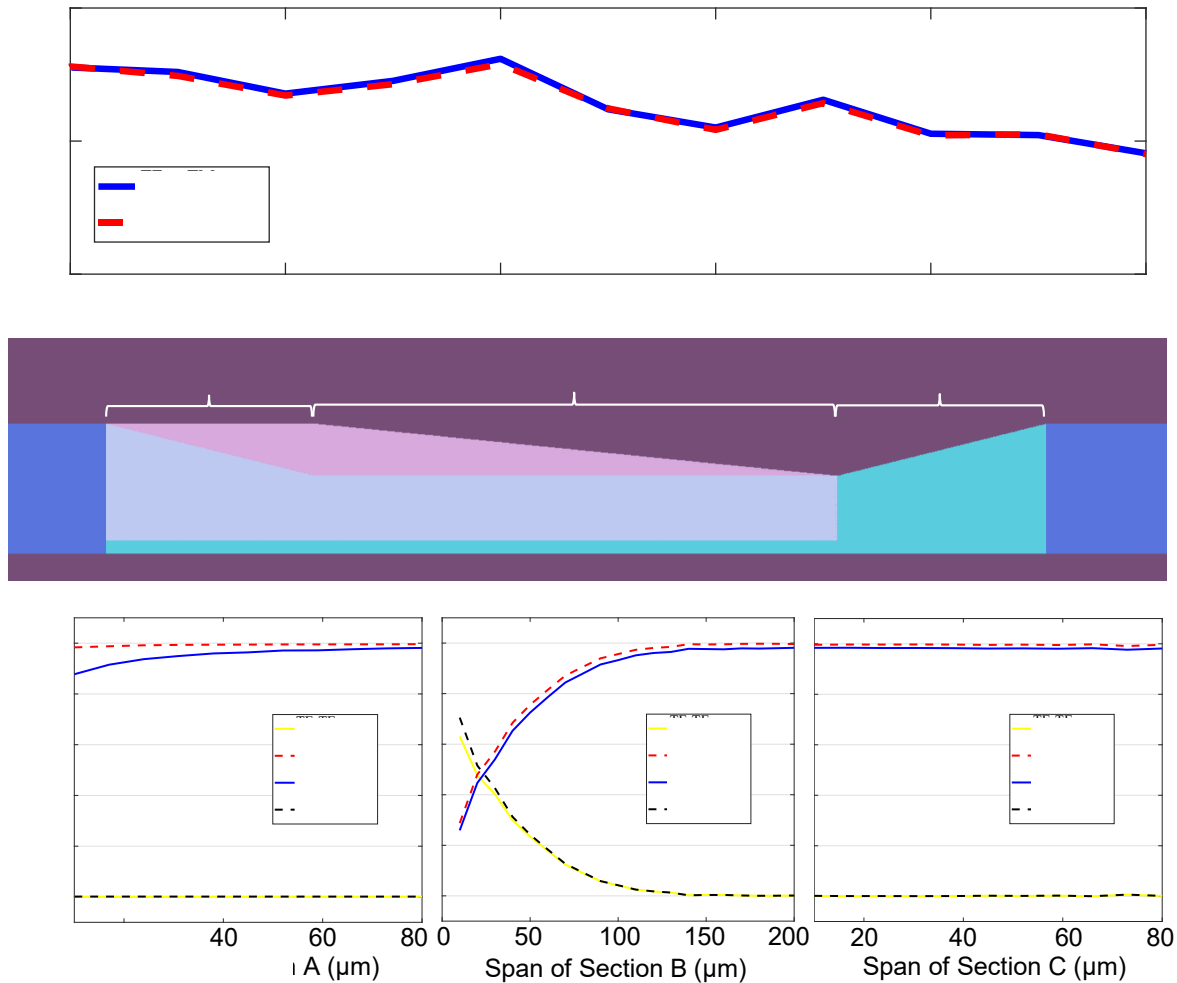


Supplementary Figure 1 | Design map for the silicon integrated photonics PC-NOT gate.

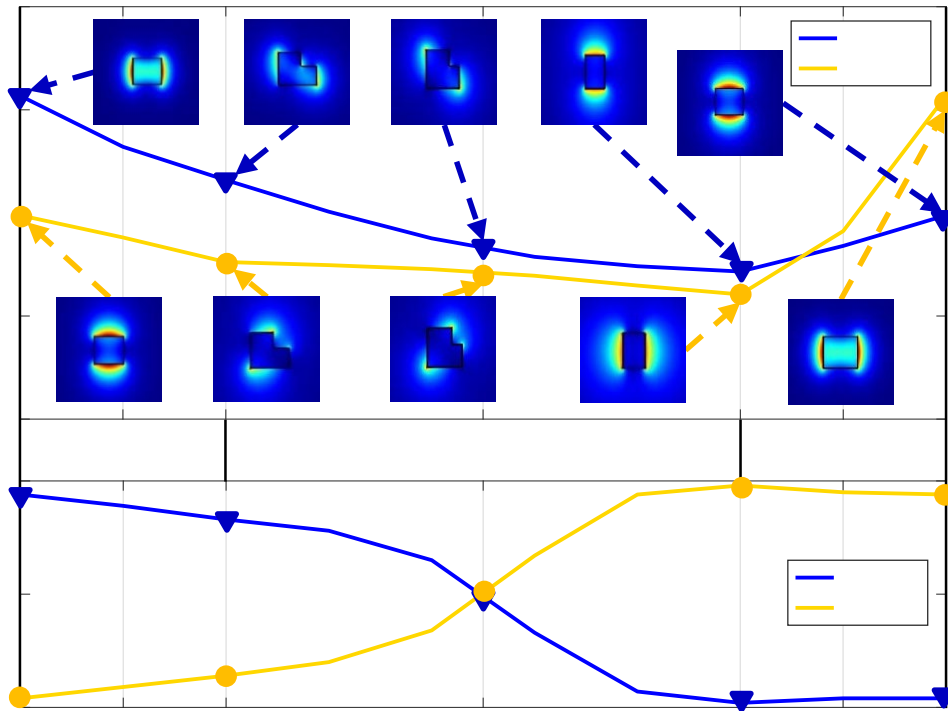
Cross-over coupling length versus waveguide and gap widths of the TE (a) and TM (b) modes. Fraction of the energy coupled to the cross-channel versus coupler length and gap width for TE (c) and TM (d) modes with a waveguide width of 460 nm. The thickness of the device is fixed at 220 nm. The red circle denotes the designed and fabricated device choice.

I.B. MC-NOT gate design and implementation: The design for the MC-NOT gate is based on a silicon integrated photonics two-level polarization rotator [S6]. The polarization rotator was designed with a silicon thickness of 220 nm and analyzed through eigenmode expansion simulations. As shown in Supplementary Figure 2b, the designed polarization rotator consists of a polarization rotation section (A and B) and a mode conversion section (C). Sections A and B are asymmetric rib waveguides that rotate the polarization angle of the waveguide mode, and Section C is a nano-tapered waveguide in which the polarization of the local mode is maintained. The length of each section is varied independently to obtain the best conversion efficiency. This continuous waveguide structure prevents extra loss induced by the mode mismatch, which is

crucial to implementing a low-loss polarization rotator. The conversion efficiency of each section is evaluated by a detailed propagation analysis using the FDTD method, with the results versus length shown in Supplementary Figure 2c. Optimal conversion efficiency of each section is obtained with the lengths set to 80 μm , 200 μm and 80 μm for sections A, B and C, respectively. With the optimized waveguide structure, the extinction ratio for the polarization rotation operation was examined across different wavelengths to determine the optimal operating wavelength for the SWAP gates, as shown in Supplementary Figure 2a.



Supplementary Figure 2 | Design map for the silicon integrated photonics MC-NOT gate. a, Extinction ratio of the MC-NOT gate versus operation wavelength for both TE-to-TM and TM-to-TE mode conversions. **b,** Top view of the MC-NOT gate's design model. **c,** Conversion efficiency changes along the length for each individual section of the MC-NOT gate.



Supplementary Figure 3 | Local mode analysis of the silicon integrated photonics MC-NOT gate. a, Effective refractive indices of the two local modes along the device. Inset: *E*-field profiles of two modes at different positions in each section. **b,** TE polarization fraction for the two local modes along the MC-NOT gate.

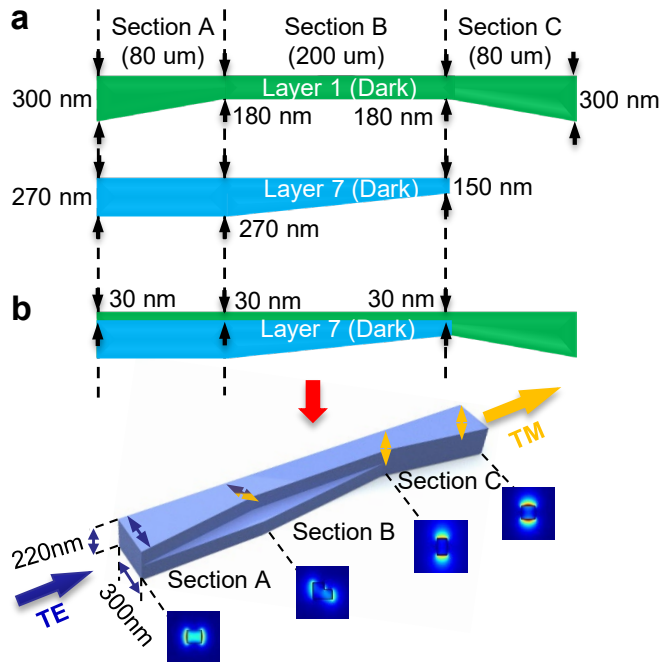
The final design was examined by monitoring the fundamental TE and TM modes throughout the device using eigensolver analysis. The evolution of the effective refractive indices and polarization states (TE fraction) of the two local modes are illustrated in Supplementary Figure 3. The inset of Supplementary Figure 3 depicts the *E*-field intensity for each mode. At the input to section A, there are two local modes A and B with TE-like and TM-like polarizations, respectively. The input TE-like mode couples to mode A and the TM-like mode couples to mode B. The polarization direction is gradually rotated along the waveguide from section A to B due to the asymmetry in both horizontal and vertical directions of the waveguide. The continuous change of the TE fraction also specifies the polarization rotation. The polarization directions of the local modes are continuously rotating and achieve 90° rotation at the output of section B. Despite that, the TE fractions for modes A and B are the same at the midpoint of section B, with the polarization

directions of modes A and B being perpendicular at this point, as depicted in the insets of Supplementary Figure 3a. Under adiabatic conditions, only one of modes A or B is excited, preventing their mixing and thus ensuring high conversion efficiency. Two local modes continue to propagate through section C without polarization rotation, and they are converted to the input mode set because the waveguide cross section of section C is the same as section A's. At this point, polarization rotation is complete. We also note that the sidewall roughness in near the neck region of section B or at the beginning of section C will result in the TE and TM modes suffering different losses, because the TE-like mode is more spread out than the TM-like mode in the neck region and also more sensitive to sidewall. The loss induced by the sidewall roughness can be reduced by improving the fabrication process [S7]. The designed low-loss small-footprint polarization rotator was used for the top channel of our SWAP-gate implementation, as shown in Figure 1f, and thus works effectively as an MC-NOT gate.

II. Nanofabrication and characterization of the PC-NOT and MC-NOT gates

II.A. Nanofabrication of the silicon integrated photonics MC-NOT gate: Prior efforts to fabricate an integrated polarization rotator are described in Refs. [S8-S15]. The rotator requires two-level fabrication with two-mask alignment. Misalignment of the two masks (or levels) creates scattering losses and reduces the TM-to-TE extinction ratio, limiting the performance of the resulting MC-NOT gate and ultimately the SWAP gate. To mitigate misalignment, authors of this manuscript (M. Yu and D.-L. Kwong) developed a mask design that minimizes the ill effects of misalignment in the two-level polarization rotator [S16]. Even with this improved mask design, a ± 60 nm misalignment will decrease the extinction ratio and rotation efficiency.

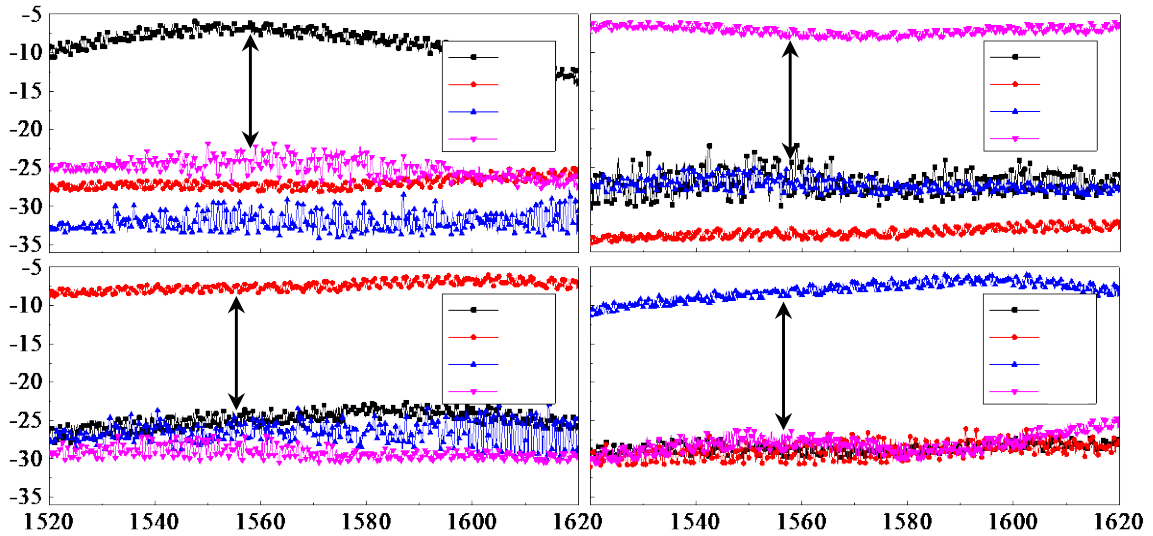
To overcome misalignment, we have developed a self-aligned two-level nanofabrication approach in order to achieve the TM-to-TE extinction ratio required for the polarization rotator, MC-NOT gate, and SWAP gate. Supplementary Figure 4a illustrates the two mask layers implemented in our tapeout. Both are dark-field masks with Layer 1 patterned in a hard mask (aluminum) and Layer 7 patterned in a photoresist. The respective dimensions of sections A, B and C are illustrated for both Layer 1 and Layer 7. Supplementary Figure 4b illustrates the combination of both mask layers which then serves as the single mask for the first 220 nm Si reactive ion etch for sections A, B and C. After this etch, the Layer 7 resist is stripped via a resist developer, leaving the already-patterned hard mask. This hard mask — already self-aligned to the first etch — serves as the mask to define the 110 nm etch for sections A and B.



Supplementary Figure 4 | Self-aligned two-level nanofabrication approach. a, Two mask layers implemented in the nanofabrication of our silicon chip’s design tapeout. Both are dark-field masks with Layer 1 patterned in a hard mask and Layer 7 patterned in a photoresist. **b**, The combination of both mask layers serves as the single mask for the first 220 nm Si reactive ion etch for sections A, B and C. This self-aligned two-level fabrication approach guarantees 30 nm layer-to-layer offset without alignment error.

Our self-alignment procedure eliminates the need for alignment between the two Si etch steps, where alignment might be difficult to achieve in the second lithography owing to the step-height relief of the Si waveguides. The only two-level alignment (Layer 7 to Layer 1) is before the first etch, with a relatively flat surface for lithography patterning. It is also easier to inspect and verify the 30 nm lateral offset via metrology, before the etch, of this relatively flat surface. To guarantee the 30 nm lateral offset between Layer 1 and Layer 7 (as shown in Supplementary Figure 4a), the second lithography resist pattern is inspected after lithography and patterning across the whole wafer. If any 30 nm offset across the whole 8-inch wafer span deviates by more than ± 60 nm, the resist is stripped and the second lithography step is repeated until a more uniform 30 nm lateral offset is obtained. In this foundry cleanroom, our two-level alignment’s accuracy is guaranteed within ± 60 nm bounds across the entire wafer. Resulting detailed measurements of the nanofabricated two-level MC-NOT gate will be described below in Supplementary Section II.C.

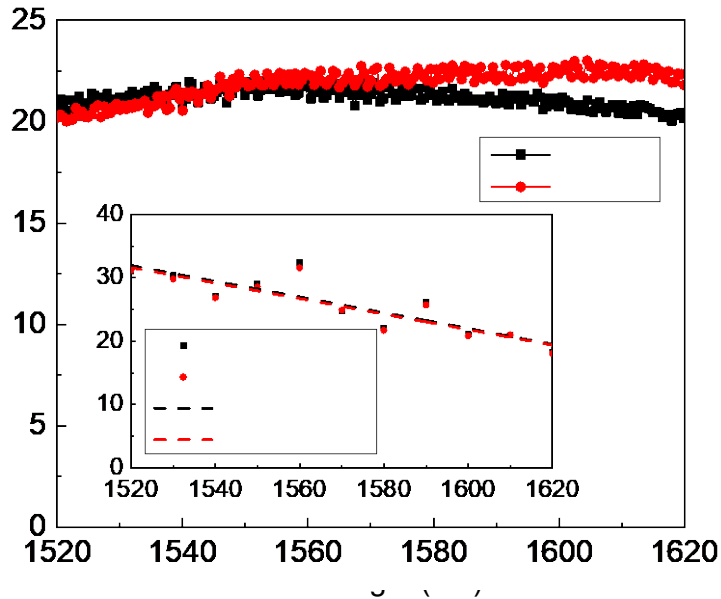
II.B. Characterization of the PC-NOT gate: To test the performance of each logical operation within our SWAP gate, we performed classical transmission measurements on the individual PC-NOT and MC-NOT gates separately. The PC-NOT gate’s transmission spectrum was measured with a swept C-band tunable laser (Santec-510) via a 2×2 input-output free-space coupling system that selects the PC-NOT gate’s top and bottom channels for its input and output. The input light’s polarization is set by a polarizer and a half-wave plate, and the output light is measured using a polarizer. The transmission for different input/output polarization and channel combinations at different wavelengths is shown in Supplementary Figure 5. We obtained an average extinction ratio (for the desired output of the corresponding input) of more than 18 dB between 1520 nm to 1620 nm, which confirms the good overall performance of the PC-NOT gate.



Supplementary Figure 5 | Characterization of the silicon integrated photonics PC-NOT gate. Classical transmission measurements between different input-output ports and polarization combinations, along with wavelength characterization over 100 nm. Good overall performance of more than 18-dB extinction ratio is achieved in the C-band.

II.C. Characterization of the MC-NOT gate: The MC-NOT gate’s performance was characterized by classical transmission measurements for different input polarizations. The swept C-band tunable laser was linearly polarized by an input polarizer to excite TE-like and TM-like modes (described earlier in Supplementary Information Section I.B) at the input of the silicon waveguide. For both polarization characterization measurements, polarized light is input from the same side of the waveguide and the output light is measured by adjusting the polarization axis of

the output polarizer. Supplementary Figure 6 shows the measured extinction ratio of the MC-NOT gate. We obtain an extinction ratio of more than 20 dB in the C-band, agreeing well with our numerical simulations for the polarization-conversion extinction ratios (shown in Supplementary Figure 6 inset). This extinction value is mainly limited by the alignments of rotation angles between the collimating fibers and the waveguide. These good performance characteristics of the individual PC-NOT and MC-NOT gates bode well for the overall SWAP operation that is realized with the PC-NOT, MC-NOT, PC-NOT cascade.

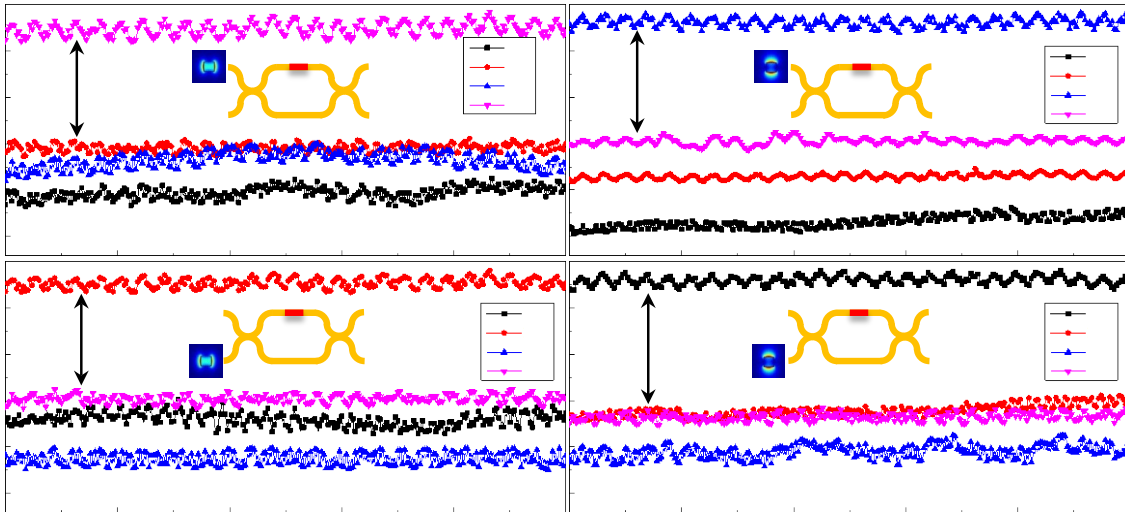


Supplementary Figure 6 | Characterization of the silicon integrated photonics MC-NOT gate. Measured extinction ratios of the MC-NOT gate obtained by wavelength scanning across a 100-nm spectrum. Inset: extinction-ratio modeling the MC-NOT gate across a 100-nm spectrum.

III. Spectral and cross-talk characterization of the on-chip SWAP gate

Supplementary Figure 7 summarizes the cross-talk characterization of the SWAP gate, with 16 input-output states and for wavelengths from 1550 nm to 1560 nm. We characterized the SWAP gate architecture with a swept C-band tunable laser (Santec TSL-510). Input polarization states were prepared with bulk optics and fed to the SWAP gate chip through a 2-in 2-out free-space fiber coupling system to access the top and bottom channels. Thus, the cross-talk of the SWAP gate was characterized for the four-basis states: $|TH\rangle$, $|TV\rangle$, $|BH\rangle$ and $|BV\rangle$. Consistent performance was achieved from 1550 nm to 1560 nm with extinction ratios of more than 12 dB obtained for all four inputs. Spectral [oscillations](#) were observed due to laser [polarization](#) instability,

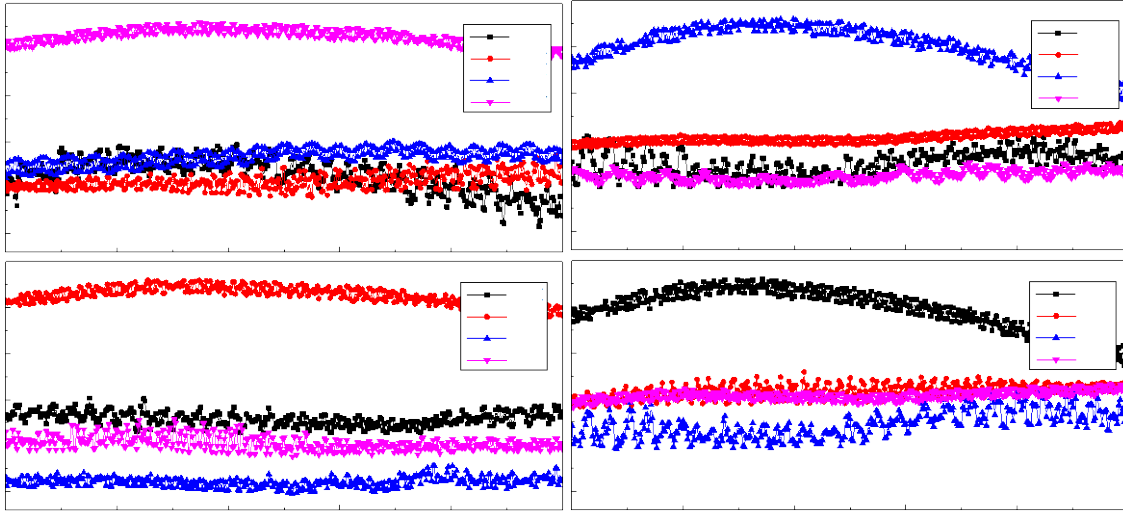
uneven waveguide coupling misalignment at different wavelengths, and [the possible Fabry-Pérot reflections at the input and output facets](#). The extinction ratio of the SWAP gate is mainly bounded by the finite extinction ratios of the PC-NOT and MC-NOT gates, and by the polarization misalignment between the output waveguide mode and the projection polarizers. These limits are due to imperfect fabrication and waveguide surface and sidewall roughness, resulting in propagation loss and impure optical modes. Higher extinction ratios can be realized by using a better fabrication process [S7, S17, S18].



Supplementary Figure 7 | Characterization of cross-talk suppression in the SWAP gate, for 16 input-output state combinations. Measurements were taken from 1550 nm to 1560 nm, covering the $|T\rangle$, $|B\rangle$, $|H\rangle$, $|V\rangle$ combinations. At least 12 dB cross-talk suppression was observed across all states, and was bounded primarily by the finite polarization extinction ratio in the PC-NOT and MC-NOT gates.

In Supplementary Figure 8 we illustrate the broader-band 100-nm transmission spectrum of the SWAP gate (using another device on the same chip), from 1520 nm to 1620 nm. Good performance can still be achieved in the optical telecommunications C-band with more than 12 dB cross-talk suppression. The four-basis state cross-talk arises mainly from the finite polarization extinction ratio of the PC-NOT and MC-NOT gates. The decreased cross-talk suppression at longer wavelengths is attributed to the free-space to chip coupling falloff at those wavelengths. The chip's insertion loss is related to fabrication defects and waveguide surface roughness, which

affect the coupling and transmission losses. The total (input-chip-output) insertion loss can be further reduced to below 6 dB by better engineering of the coupler structure.



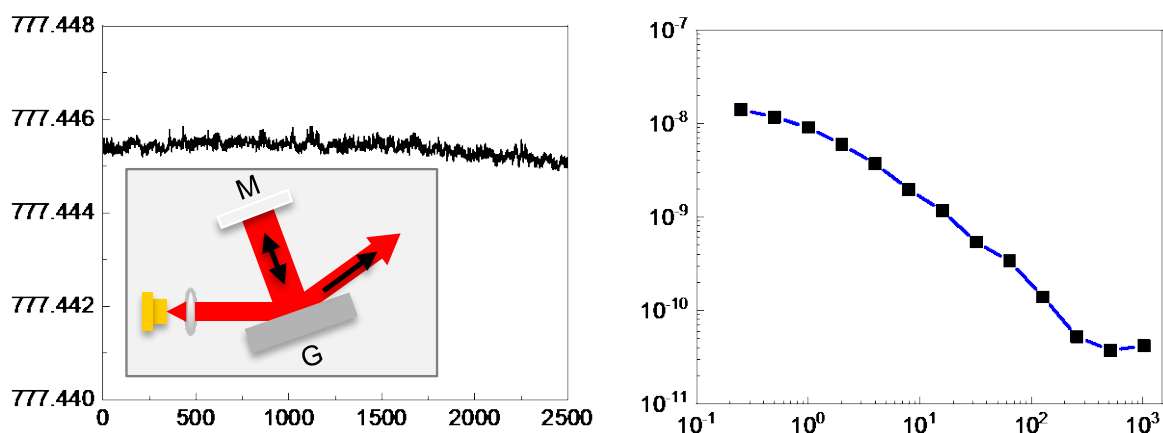
Supplementary Figure 8 | Cross-talk characterization between different input-output ports and polarization combinations scanning across 100 nm spectrum. Within the optical communications C-band (1530 nm to 1565 nm), a cross-talk suppression of more than 12 dB is obtained across the four bases in our silicon SWAP gate.

IV. Double-pass self-injection-locked pump laser

In order to evaluate the wavelength dependence and operating bandwidth of our on-chip SWAP gate, the pump laser needs to a relatively narrow linewidth and spectrally stable for the type-II phase-matched spontaneous parametric downconversion (SPDC) process to generate narrowband, tunable, heralded single-photons. Pump light at 777 nm can be easily obtained from a Fabry-Pérot laser diode. However, conventional Fabry-Pérot laser diodes tend to have multi-longitudinal mode lasing output, and the spectrum is not stable because of longitudinal-mode competition. Therefore, a self-injection locked laser was built using external grating feedback for wavelength stabilization. The inset in Supplementary Figure 9a shows our pump laser setup. The light from the Fabry-Pérot laser diode was collimated and directed toward a diffraction grating. Similar to the Littman-Metcalf configuration in an external-cavity diode laser setup, a double-pass optical feedback loop was implemented with the diffraction grating, where the first-order diffraction is fed back via a high-reflection mirror M for wavelength locking. The zeroth-order diffraction was used as the laser

output. As a result, single longitudinal-mode lasing is achieved, and the laser wavelength is tunable within the diode’s gain bandwidth by changing the mirror angle.

For coincidence-counting measurements, the pump laser should be stable during long integration times. We studied the pump wavelength stability using a wavelength meter (821-IR wavemeter, Bristol Instruments Inc.). As shown in Supplementary Figure 9a, the pump wavelength stays within less than 1 pm drift during 2,500 seconds, with a small drift slope. The fractional frequency Allan deviation of the self-injection locked pump laser carrier frequency is also depicted in Supplementary Figure 9b. The Allan deviation was found to be 9×10^{-9} in 1s, and gradually decreased to 4.2×10^{-11} in 1,000 s. In summary, we achieved a wavelength-stabilized heralded single-photon source suitable for SWAP-gate characterization thanks to our self-injection locked pump laser.

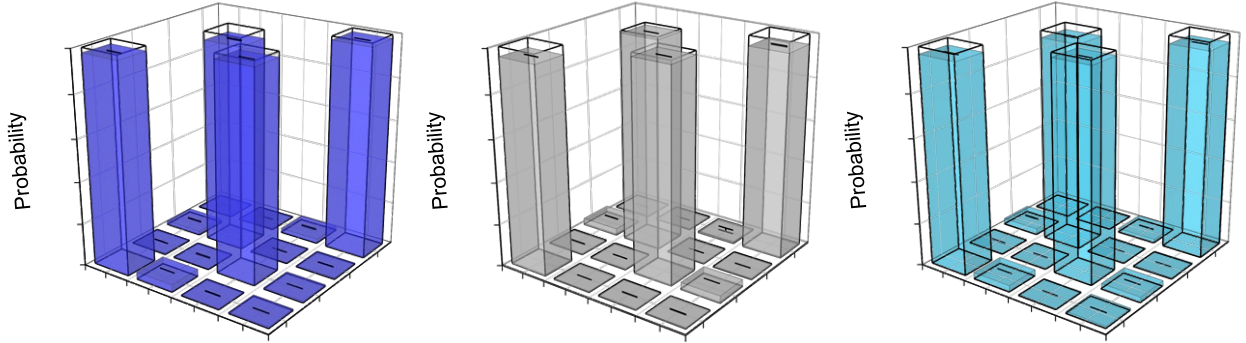


Supplementary Figure 9 | Stabilized 777 nm pump laser with self-injection locking. a, Long-term wavelength stability measurement of the 777 nm pump laser. Inset: layout schematic of our custom-built 777 nm stabilized laser. LD: 780 nm Fabry-Pérot laser diode with temperature stabilization; L: collimating lens; G: diffraction grating; M: high-reflection mirror. **b**, Fractional frequency Allan deviation of the self-injection locked 777 nm pump laser over measurement time τ .

V. Truth table of SWAP gate at different wavelengths

Truth tables are measured at different wavelengths to examine the consistent performance of our on-chip SWAP gate in the logical basis. By tuning the wavelength of the self-injection locked pump laser, we are able to generate SPDC photons at different wavelengths. We measure the truth

table with signal photons at 1556 nm, 1557 nm, and 1558 nm, respectively, as the input single photons, and collect the coincidence counts heralded by the idler photons. A total of around 100,000 coincidence counts is obtained for each truth table measurement using the measurement scheme shown in Figure 2a (I). Supplementary Figure 10 shows the truth table measured at different wavelengths, with a wavelength-averaged truth table fidelity of $97.2 \pm 0.1\%$. The consistent truth table fidelities measured in the logical basis agree with the broadband performance from the transmission measurements in Supplementary Information Sections III.



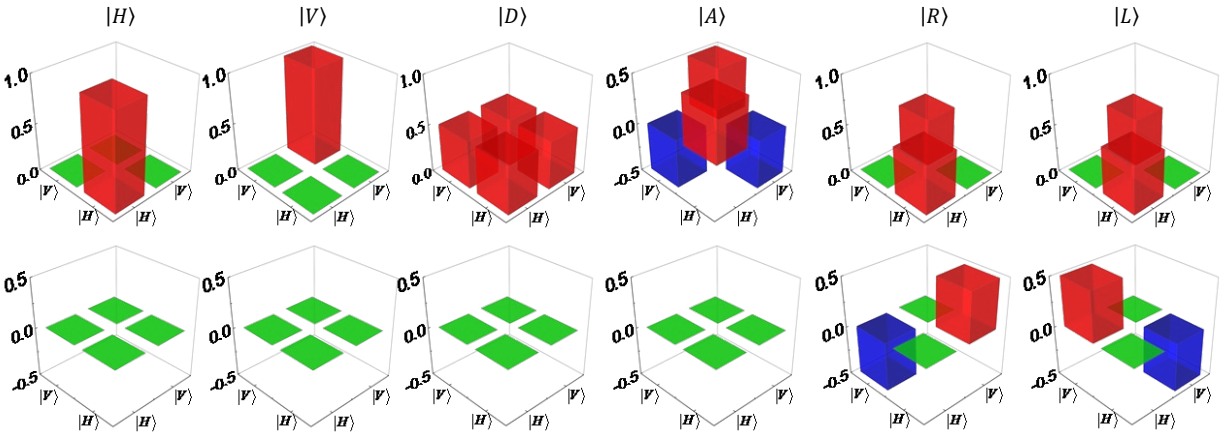
Supplementary Figure 10 | Truth tables of the on-chip SWAP gate in computational basis at different wavelengths. Fidelities of the measured truth tables are $97.4 \pm 0.1\%$ at 1556 nm, $97.4 \pm 0.2\%$ at 1557 nm, and $96.9 \pm 0.1\%$ at 1558 nm, yielding a wavelength-averaged fidelity $\bar{F}_{gate,truth}$ of $97.2 \pm 0.1\%$, in support of the excellent performance in the logical basis.

VI. Quantum state tomography for single-qubit and two-qubit SWAP operation

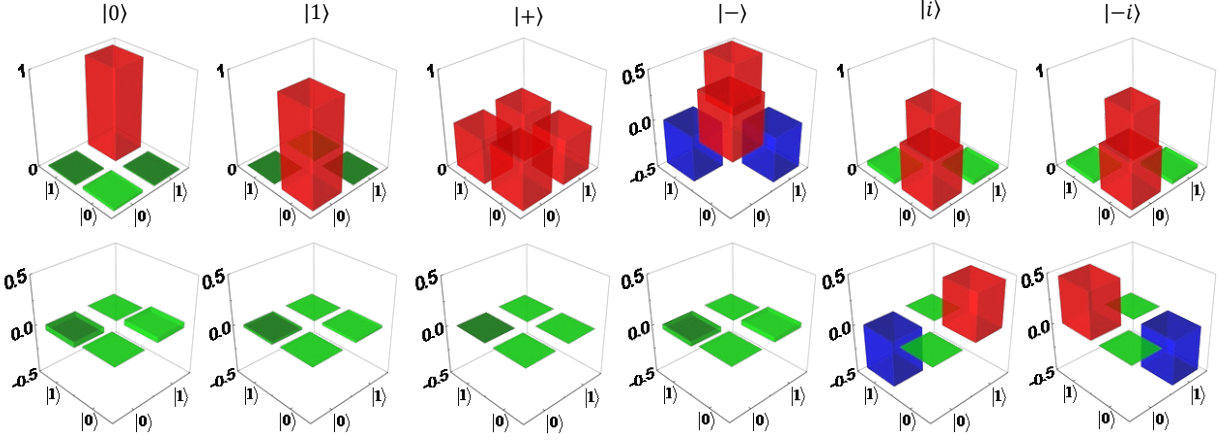
VI.A. Single-qubit quantum state tomography: A set of six polarization-encoded states ρ_{pol} — $|H\rangle, |V\rangle, |D\rangle = (|H\rangle + |V\rangle)/\sqrt{2}, |A\rangle = (|H\rangle - |V\rangle)/\sqrt{2}, |R\rangle = (|H\rangle + i|V\rangle)/\sqrt{2}, |L\rangle = (|H\rangle - i|V\rangle)/\sqrt{2}$ — are first prepared by free-space half-wave and quarter-wave plates and fed into the top or bottom channel of the on-chip SWAP gate for quantum state tomography. For each input-polarization state, we analyze the corresponding output spatial-momentum encoded states ρ_{sm} in six basis states $|0\rangle, |1\rangle, |+\rangle = (|0\rangle + |1\rangle)/\sqrt{2}, |-\rangle = (|0\rangle - |1\rangle)/\sqrt{2}, |+i\rangle = (|0\rangle + i|1\rangle)/\sqrt{2}, |-i\rangle = (|0\rangle - i|1\rangle)/\sqrt{2}$ by projecting them onto a custom-built Mach-Zehnder interferometer (MZI) with over 20 dB extinction ratio. The custom-built MZI consists of two tunable delay lines, with the first delay line placed before the input of the MZI to tune the relative phase between the two output spatial-momentum modes from the SWAP gate. The second delay line was inserted into the upper arm of the MZI to tune the relative delay between the two arms of

the MZI. The six spatial-momentum encoded states were calibrated by tuning the two delay lines and measuring the powers from the two output ports of the MZI. We set φ_1 and φ_2 as the relative phases tuned by the first and second delay lines. We define each of the six spatial-momentum encoded states with relative phase φ_1 and φ_2 as: $|0\rangle$ when $\varphi_1=0$ and $\varphi_2=0$, $|1\rangle$ when $\varphi_1=\pi$ and $\varphi_2=0$, $|+\rangle$ when $\varphi_1=\pi/2$ and $\varphi_2=0$, $|-\rangle$ when $\varphi_1=-\pi/2$ and $\varphi_2=0$, $|i\rangle$ when $\varphi_1=\pi/2$ and $\varphi_2=\pi/2$, $| - i\rangle$ when $\varphi_1=\pi/2$ and $\varphi_2=-\pi/2$.

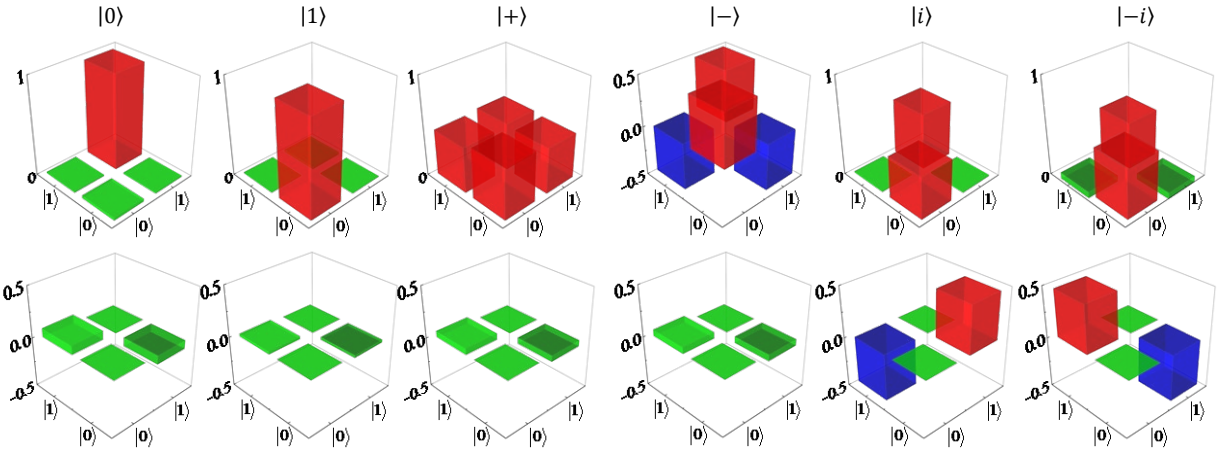
The density matrix for each output spatial-momentum state is reconstructed using a maximum-likelihood algorithm to obtain the most likely legitimate state from the measurements [S19]. After the density matrix is retrieved, we can extract the fidelity of the measured state. The fidelity describes the overlap between the measured state and the ideal theoretical one, and is defined as $F = (\text{Tr}(\sqrt{\sqrt{\rho_{pol}}\rho_{sm}\sqrt{\rho_{pol}}}))^2$. Fidelity of unity corresponds to a perfect overlap between the output spatial-momentum states and the input polarization states. Supplementary Figure 11 shows the ideal input polarization states ρ_{pol} prepared by bulk optics, and Supplementary Figures 12-15 illustrate the measured spatial-momentum encoded states ρ_{sm} for the $|T\rangle$, $|B\rangle$, $|+\rangle$ and $|+i\rangle$ spatial-momentum input states, respectively.



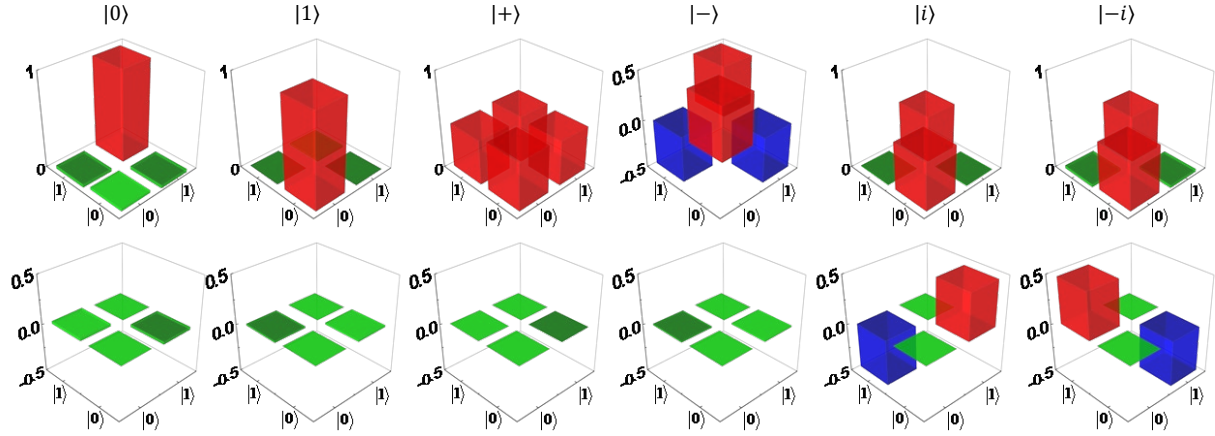
Supplementary Figure 11 | Density matrix of ρ_{pol} ideal polarization-encoded states $|H\rangle$, $|V\rangle$, $|D\rangle$, $|A\rangle$, $|R\rangle$ and $|L\rangle$, prepared by bulk optics.



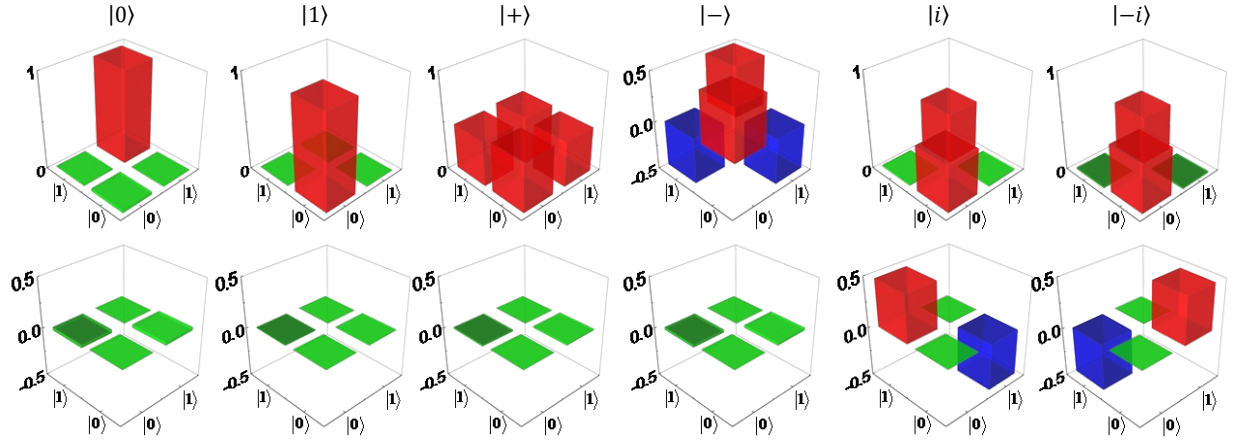
Supplementary Figure 12 | Real (top) and imaginary (bottom) part of the reconstructed density matrix ρ_{sm} of measured spatial-momentum encoded states $|0\rangle$, $|1\rangle$, $|+\rangle$, $|-\rangle$, $|+i\rangle$ and $| -i\rangle$ for $|T\rangle$ input states. The state fidelities between ideal ρ_{pol} and measured ρ_{sm} are calculated to be 97.2%, 97.6%, 96.7%, 97.3%, 97.5% and 97.2% respectively.



Supplementary Figure 13 | Real (top) and imaginary (bottom) part of the reconstructed density matrix ρ_{sm} of measured spatial-momentum encoded states $|0\rangle$, $|1\rangle$, $|+\rangle$, $|-\rangle$, $|+i\rangle$ and $| -i\rangle$ for $|B\rangle$ input states. The state fidelities between ideal ρ_{pol} and measured ρ_{sm} are calculated to be 97.9%, 97.3%, 97.0%, 97.3%, 97.6% and 97.2% respectively.



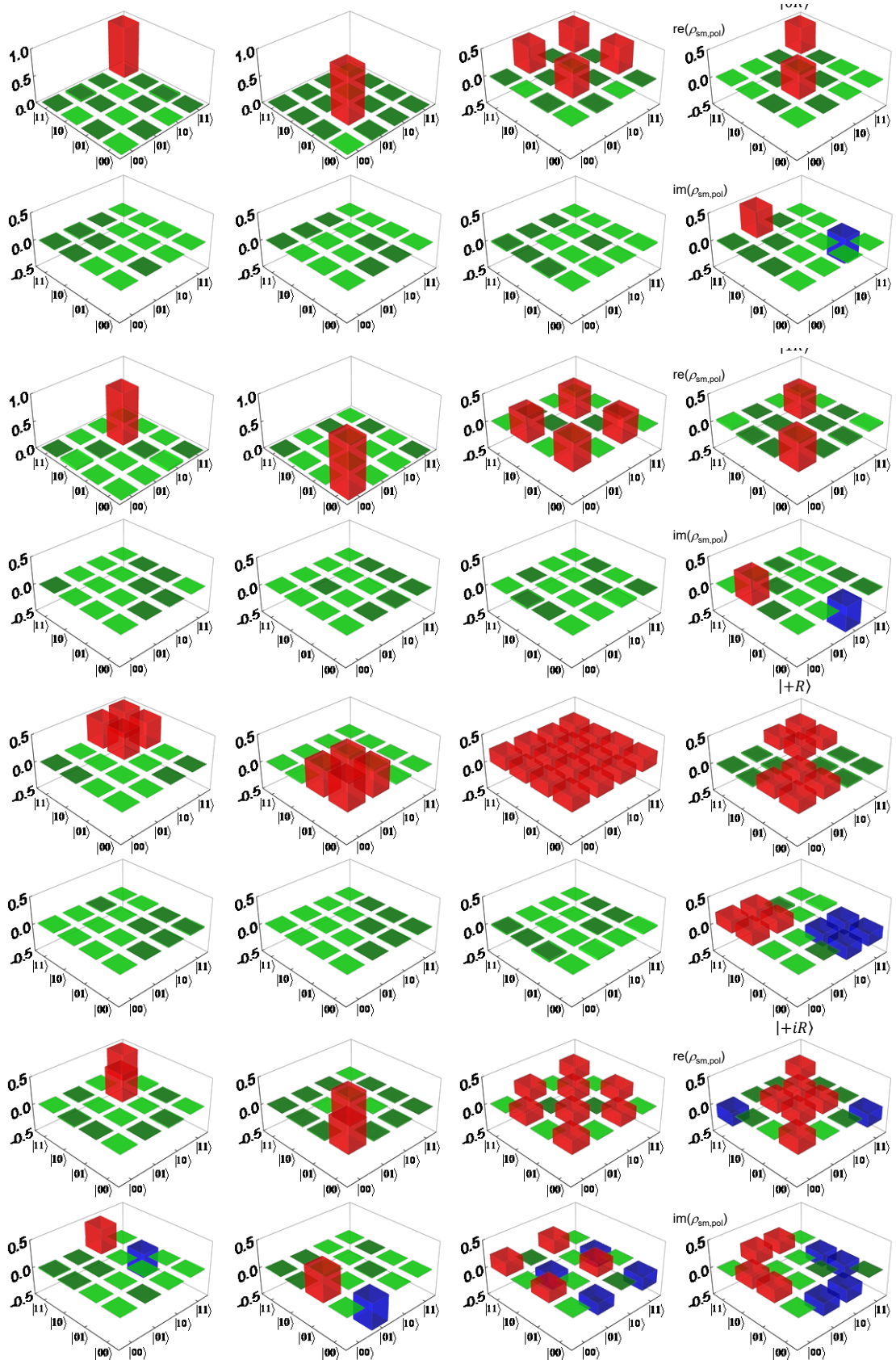
Supplementary Figure 14 | Real (top) and imaginary (bottom) part of the reconstructed density matrix psm of measured spatial-momentum encoded states $|0\rangle$, $|1\rangle$, $|+\rangle$, $|-\rangle$, $|+i\rangle$ and $| -i\rangle$ for $|+\rangle$ input states. The state fidelities between ideal ppol and measured psm are calculated to be 97.2%, 97.5%, 96.7%, 97.1%, 97.2% and 97.0% respectively.



Supplementary Figure 15 | Real (top) and imaginary (bottom) part of the reconstructed density matrix psm of measured spatial-momentum encoded states $|0\rangle$, $|1\rangle$, $|+\rangle$, $|-\rangle$, $|+i\rangle$ and $| -i\rangle$ for $|+i\rangle$ input states. The state fidelities between ideal ppol and measured psm are calculated to be 97.0%, 97.2%, 96.9%, 96.9%, 97.0% and 96.8% respectively.

VI.B. Two-qubit quantum state tomography: For two-qubit operation of the on-chip SWAP gate, additional to the setup shown in Figure 2a (II), we inserted waveplates and polarizers before the MZI at the output of the chip for the polarization qubit analysis. 16 separable, linearly independent states $\rho_{sm,pol} = |i_{sm}j_{pol}\rangle$ are prepared as input two-qubit states, where $i_{sm} = 0, 1, +, +i$ and $j_{pol} = H, V, D, R$. The output states are projected in the same set of 16 state basis $\{|0H\rangle, |0V\rangle, |0D\rangle, |0R\rangle, |1H\rangle, |1V\rangle, |1D\rangle, |1R\rangle, |+H\rangle, |+V\rangle, |+D\rangle, |+R\rangle, |+iH\rangle, |+iV\rangle, |+iD\rangle,$

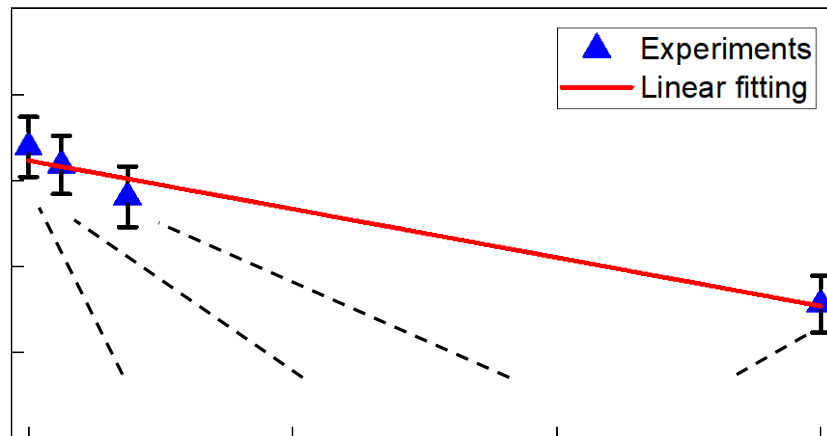
$|+iR\rangle\}$. 256 measurements are performed with different input states and measurement projections to reconstruct 16 density matrices for two-qubit quantum process tomography of our on-chip SWAP gate. Supplementary Figure 16 shows the reconstructed density matrix of the swapped output state for each input state, with an averaged state fidelity up to $96.1 \pm 0.8\%$.



Supplementary Figure 16 | Real (top) and imaginary (bottom) part of the reconstructed density matrix $\rho_{\text{sm,pol}}$ of the swapped output states for 16 different input states. The state fidelities between ideal and measured states are calculated to be 96.7%, 96.9%, 97.0%, 96.5%, 96.6%, 96.5%, 95.6%, 96.0%, 96.8%, 97.1%, 95.7%, 95.0%, 95.0%, 96.9%, 95.0%, and 94.8%, respectively.

VII. Long-term stability of polarization-spatial two-qubit self-interference measurement after the SWAP operation

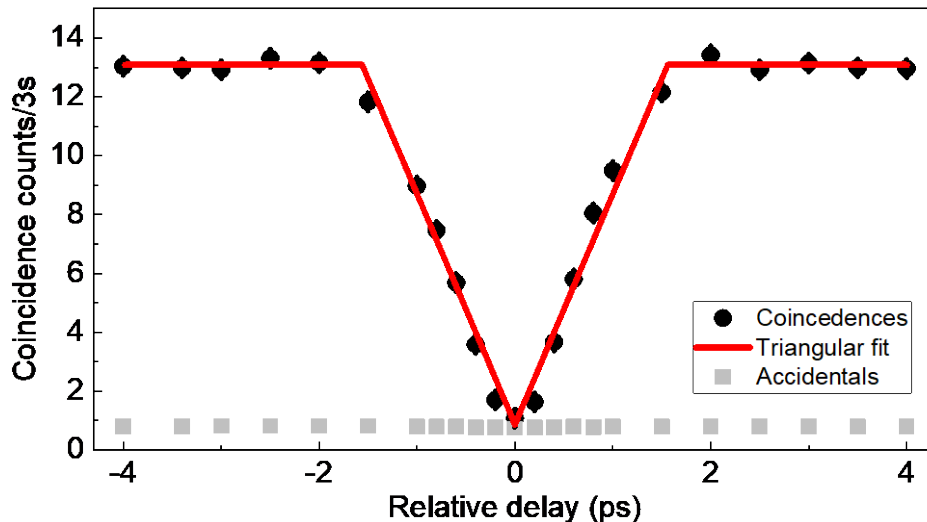
To verify the long-term stability of the phase-coherent SWAP-gate operation, we examined the single-photon two-qubit self-interference at different time scales. We measured the phase stability of the self-interference fringes for the $|T\rangle$ channel input using the experimental scheme shown in Figure 2 (III) in the main text and collected the coincidence counts after 1, 3 and 24 hours, respectively. Supplementary Figure 17 shows the long-term measurements results, free-running and without feedback stabilization, with $98.6 \pm 0.4\%$, $98.2 \pm 0.3\%$, $97.8 \pm 0.4\%$, and $96.6 \pm 0.3\%$ visibilities at 0-hour, 1-hour, 3-hour, and 24-hour respectively. The self-interference fringe visibility only drops 2.08% after 24 hours. This demonstrates robust coherent phase-preserving SWAP-gate operation.



Supplementary Figure 17 | Long-term stability of phase coherence measurement with arbitrary input-polarization qubit at 1558 nm. The data points are fringe visibilities without background subtraction, and presented as mean values +/- SD with $n = 3$. The red solid line is the numerical fit. Error bars are given by one standard deviation assuming Poissonian statistics with three sets of measurements.

VIII. Hong-Ou-Mandel interference of the biphotons from the SPDC source

The indistinguishability of the biphotons from the SPDC source is examined by Hong-Ou-Mandel (HOM) interferometer consisting of a fiber beamsplitter and an optical delay line. The signal and idler photons are separated by a PBS and then enter a fiber 50:50 beamsplitter from different sides. A fiber polarization controller on one arm of the HOM interferometer controls the polarization angle so that the signal and idler photons will have the same polarization at the beamsplitter. A fiber tunable delay line is introduced to tune the relative delay between the two arms of the interferometer to find the optimal temporal overlapping between signal and idler photons. The HOM interference dip is obtained by scanning the relative delay between two arms of the interferometer as shown in Supplementary Figure 18. We obtained a HOM visibility of $97.9 (93.4) \pm 1.0\%$ after (before) background subtraction. The base-to-base dip width indicates the two-photon coherence time of the SPDC photon pairs, which is measured to be 3.15 ± 0.02 ps, corresponding to a two-photon bandwidth of 317 ± 2 GHz.

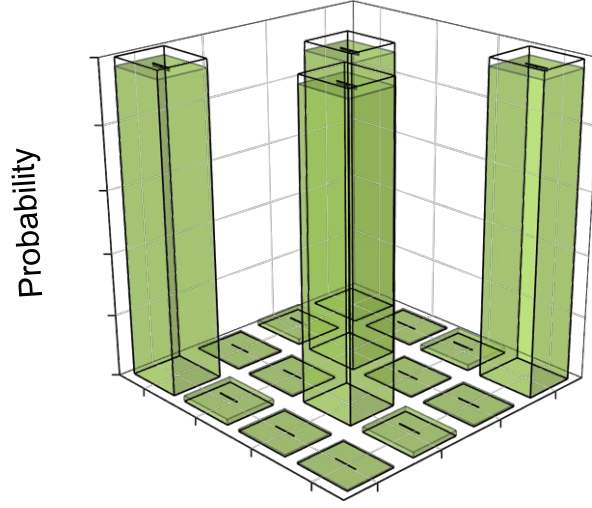


Supplementary Figure 18 | Hong-Ou-Mandel interference of the photon pairs from SPDC source. The Hong-Ou-Mandel interference visibility is measured to be $97.9 (93.4) \pm 1.0\%$ after (before) background subtraction.

IX. Truth table measurement of the second on-chip SWAP gate

The truth table of the second SWAP gate for chip-to-chip interconnect is measured using the same experimental setup shown in Figure 2a (I). Each projection measurement takes 10 seconds, and a total of around 100,000 coincidence counts is recorded to construct the truth table. The

measured truth table yields a fidelity $\bar{F}_{gate,truth}$ of $97.2 \pm 0.3\%$, with similar performance compared to the first SWAP gate characterized in the main text.

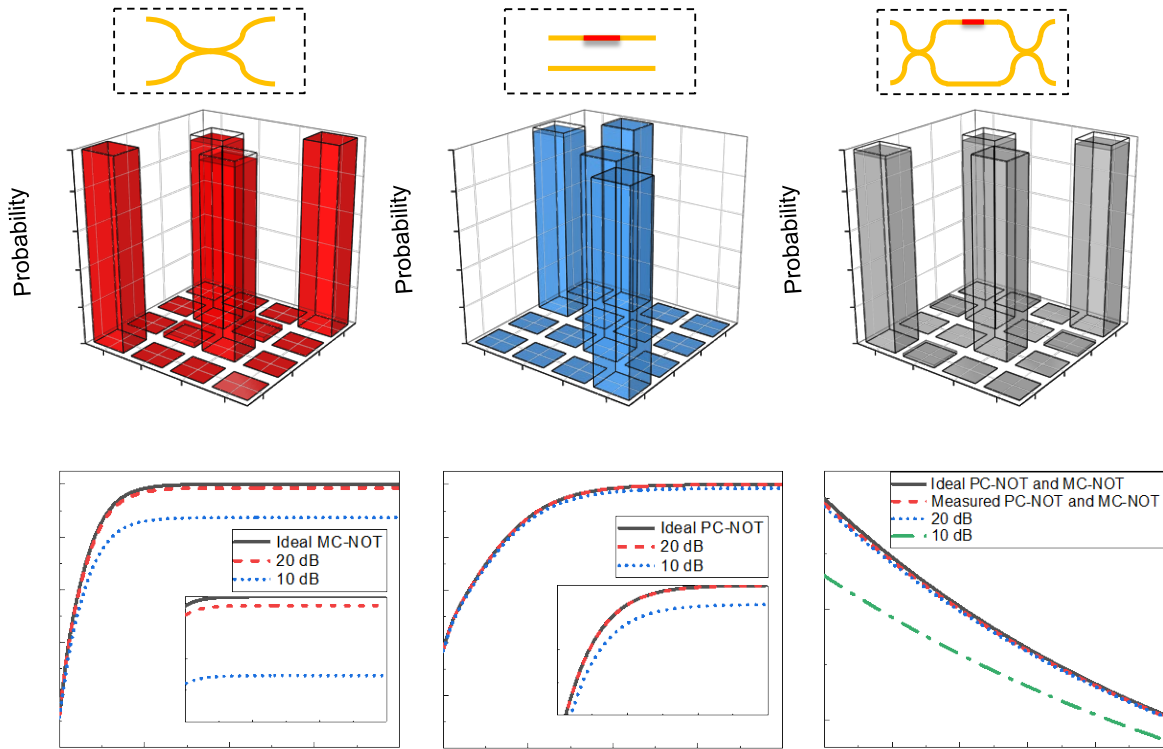


Supplementary Figure 19 | Measured truth table of the second on-chip SWAP gate. A truth table fidelity $\bar{F}_{gate,truth}$ of $97.2 \pm 0.3\%$ is obtained. The solid bars (transparent bars) represent the measured (ideal) truth table in the computational basis. A total of around 100,000 coincidence counts is recorded in 160 secs for each truth table measurement.

X. Impact of imperfect qubit rotation, spatial-mode contamination, and unbalanced photon loss on the SWAP gate’s fidelity

In order to improve our SWAP gate’s performance in pursuit of near-unity gate fidelity, we analyzed the impact on fidelity of imperfect qubit rotation, spatial-mode contamination from cross-polarization suppression, and unbalanced photon loss. First, we used the simulation results from Supplementary Section I to model the truth tables of our PC-NOT, MC-NOT and SWAP gates. These are shown in Supplementary Figures 20a-20c, respectively. According to our SWAP gate design parameters, we predict average gate fidelities of 98.64% for our PC-NOT gate, 99.27% for our MC-NOT gate and 98.23% for our SWAP gate. We also plot the gate fidelities as a function of the extinction ratios of the PC-NOT and MC-NOT gates in Supplementary Figures 20d and 20e, based on the transformation matrix model. We define output states as $Output = M_{PC} \times M_{MC} \times M_{PC} \times Input$, where M_{PC} and M_{MC} are the transformation matrices of the PC-NOT and MC-NOT gates, respectively. The modelled fidelities are calculated for various extinction ratios of the PC-NOT and MC-NOT gates. According to the characterization of individual PC-NOT and MC-NOT gates in Section II.B and II.C, we can calculate the modelled fidelities with the measured

extinction ratio of each gate. With the measured extinction ratio of 19.1 dB for the PC-NOT gate, we obtained a modelled fidelity of 98.8% for the SWAP gate operation; with the measured extinction ratio of 22.0 dB for the MC-NOT gate, we estimated a SWAP gate fidelity of 99.7%. Both fidelities are calculated while assuming other components are perfect at between 1556 nm and 1558 nm. Here, we also plot the fidelities as a function of the photon loss of the MC-NOT gate in Supplementary Figure 20f. Taking account of the imperfect extinction ratios of each individual C-NOT gate and the unbalanced loss, we estimated a gate fidelity of 97.7% assuming 0.2 dB photon loss of the MC-NOT gate, agreeing well with the experimental results shown in Figure 3a ($97.2 \pm 0.1\%$). We attribute the $\sim 0.5\%$ fidelity imperfection to the photon loss of the silicon waveguide and the coupling efficiency difference between different input and output states.



Supplementary Figure 20 | Fidelity modelling for SWAP input-output gate fidelity vs. TE-TM extinction ratios of the PC-NOT and MC-NOT gates, and loss of the MC-NOT gate. a-c, Truth tables calculated for the PC-NOT, MC-NOT and SWAP gates, based on the simulation results in Supplementary Section II, yields average gate fidelities of 98.64%, 99.27% and 98.23%, respectively. **d-e,** The modelled fidelities versus the PC-NOT gates' extinction ratio for various MC-NOT gate extinction ratios, and the MC-NOT gate's extinction ratio for various PC-NOT gate

extinction ratios. Inset is the zoom-in view near the high-fidelity region. **f**, Modelled fidelities as functions of photon loss of MC-NOT gate for different extinction ratios of the PC-NOT and MC-NOT gates. Based on our device characterization results in Section. II, we calculated average gate fidelity of 97.70% for four-basis input states, assuming 0.2 dB photon loss from the MC-NOT gate.

Supplementary References

- [S1] M. Fiorentino, T. Kim, and F. N. C. Wong, Single-photon two-qubit SWAP gate for entanglement manipulation, *Phys. Rev. A* **72**, 012318 (2005).
- [S2] O. Bechler, A. Borne, S. Rosenblum, G. Guendelman, O. E. Mor, M. Netser, T. Ohana, Z. Aqua, N. Drucker, R. Finkelstein, Y. Lovsky, R. Bruch, D. Gurovich, E. Shafir, and B. Dayan, A passive photon–atom qubit swap operation, *Nature Phys.* **14**, 996 (2018).
- [S3] R. Stárek, M. Mičuda, M. Miková, I. Straka, M. Dušek, P. Marek, M. Ježek, R. Filip, and J. Fiurášek, Nondestructive detector for exchange symmetry of photonic qubits, *npj Quantum Inf.* **4**, 35 (2018).
- [S4] R. Stárek, M. Miková, I. Straka, M. Dušek, M. Ježek, J. Fiurášek, and M. Mičuda, Experimental realization of SWAP operation on hyper-encoded qubits, *Opt. Express* **26**, 8443 (2018).
- [S5] M. Mičuda, R. Stárek, J. Fiurášek, and R. Filip, Decoherence-resilient linear optical two-qubit quantum gate, *Phys. Rev. Applied* **14**, 054066 (2020).
- [S6] K. Goi, A. Oka, H. Kusaka, K. Ogawa, T.-Y. Liow, X. Tu, G.-Q. Lo, and D.-L. Kwong, Low-loss partial rib polarization rotator consisting only of silicon core and silica cladding, *Opt. Lett.* **40**, 1410 (2015).
- [S7] T. Horikawa, D. Shimura, H. Okayama, S. Jeong, H. Takahashi, J. Ushida, Y. Sobu, A. Shiina, M. Tokushima, K. Kinoshita, and T. Mogami, A 300-mm silicon photonics platform for large-scale device integration, *IEEE J. Sel. Top. Quantum Electron.* **24**, 1 (2018).
- [S8] J. Zhang, T.-Y. Liow, M. Yu, G.-Q. Lo, and D.-L. Kwong, Silicon waveguide based TE mode converter, *Opt. Express* **18**, 25264 (2010).
- [S9] H. Fukuda, K. Yamada, T. Tsuchizawa, T. Watanabe, H. Shinojima, and S. Itabashi, Polarization rotator based on silicon wire waveguides, *Opt. Express* **16**, 2628 (2008).

- [S10] M. R. Watts, H. A. Haus, and E. P. Ippen, Integrated mode-evolution-based polarization splitter, *Opt. Lett.* **30**, 967 (2005).
- [S11] Y. Yue, L. Zhang, M. Song, R. G. Beausoleil, and A. E. Willner, Higher-order-mode assisted silicon-on-insulator 90 degree polarization rotator, *Opt. Express* **17**, 20694 (2009).
- [S12] H. Fukuda, K. Yamada, T. Tsuchizawa, T. Watanabe, H. Shinojima, and S. Itabashi. Silicon photonic circuit with polarization diversity, *Opt. Express* **16**, 4872 (2008).
- [S13] L. Chen, C. R. Doerr, and Y.-K. Chen. Compact polarization rotator on silicon for polarization-diversified circuits, *Opt. Lett.* **36**, 469 (2011).
- [S14] W. D. Sacher, Y. Huang, L. Ding, T. Barwicz, J. C. Mikkelsen, B. J. F. Taylor, G.-Q. Lo, and J. K. S. Poon, Polarization rotator-splitters and controllers in a Si₃N₄-on-SOI integrated photonics platform, *Opt. Express* **22**, 11167 (2014).
- [S15] J. Wang, S. He, and D. Dai, On-chip silicon 8-channel hybrid (de)multiplexer enabling simultaneous mode- and polarization-division-multiplexing, *Laser Photon. Rev.* **8**, L18 (2014).
- [S16] J. Zhang, M. Yu, G. Lo, and D.-L. Kwong, Silicon waveguide-based mode-evolution polarization rotator, *Proc. SPIE* **7719**, *Silicon Photonics and Photonic Integrated Circuits II*, 77190C (2010).
- [S17] T. Horikawa, D. Shimura, and T. Mogami, Low-loss silicon wire waveguides for optical integrated circuits, *MRS Commun.* **6**, 9 (2016).
- [S18] S. K. Selvaraja, G. Murdoch, A. Milenin, C. Delvaux, P. Ong, S. Pathak, D. Vermeulen, G. Sterckx, G. Winroth, P. Verheyen, W. Bogaerts, R. Baets, J. Van Campenhout, and P. Absil, Advanced 300-mm waferscale patterning for silicon photonics devices with record low loss and phase errors, in *Proc. Opto-Electronics and Communications Conference*, Busan, South Korea, PDP2-2 (2012).
- [S19] D. F. V. James, P. G. Kwiat, W. J. Munro, and A. G. White, Measurement of qubits, *Phys. Rev. A* **64**, 052312 (2001).
- [S20] I. L. Chuang and M. A. Nielsen, Prescription for experimental determination of the dynamics of a quantum black box, *J. Mod. Opt.* **44**, 2455 (1997)